Laboratory sources of turbulent plasma: a unique MHD plasma wind tunnel

2014 Plasma Sources Sci. Technol. 23 063001

(http://iopscience.iop.org/0963-0252/23/6/063001)

IOP Publishing Plasma Sources Science and Technology

Plasma Sources Sci. Technol. **23** (2014) 063001 (26pp) doi:10.1088/0963-0252/23/6/063001

Invited Review

Laboratory sources of turbulent plasma: a unique MHD plasma wind tunnel

M R Brown and D A Schaffner

Swarthmore College, Swarthmore, PA 19081, USA

Received 16 May 2014, revised 28 July 2014
Accepted for publication 8 August 2014
Published 8 September 2014

Abstract

Turbulence has been studied in laboratory plasmas for decades. Magnetic and electrostatic turbulence fluctuations have been implicated in degraded confinement in fusion devices so understanding turbulent transport is critical for those devices. The externally applied magnetic field in most laboratory plasmas has a strong effect on the character of the turbulence (particularly parallel and perpendicular to the applied field). A new turbulent plasma source is described with several unique features. First, the magnetohydrodynamic (MHD) wind tunnel configuration has no applied magnetic field and has no net axial magnetic flux. Second, the plasma flow speed is on the order of the local sound speed ($M = 1$), so flow energy is comparable to thermal energy. Third, the plasma β (ratio of thermal to magnetic pressure) is of order unity so thermal energy is comparable to magnetic energy. We will review sources of magnetic turbulence in laboratory plasmas and discuss the main analytical tools used in the study of plasma turbulence. Some initial results from the MHD plasma wind tunnel will be presented.

Keywords: magnetohydrodynamics, turbulence, laboratory, solar wind

(Some figures may appear in colour only in the online journal)

We present a review of laboratory sources of turbulent plasma. Our focus will be on sources of magnetic turbulence, and in particular, we will introduce a new type of turbulent plasma source called a magnetohydrodynamic (MHD) plasma wind tunnel. In section 1, we open with an introduction to turbulence, including the 1941 theory by Kolmogorov. The role of plasma turbulence in two important systems, the solar wind and fusion devices, is introduced. In section 2, we provide a pedagogical overview of the statistical analysis tools used in turbulence research. Analysis in both the time domain and space domain are covered. Examples from laboratory and space observations will be provided. In section 3, we give a survey of past turbulence experiments, with an emphasis on MHD fluctuations. Finally, we close in section 4 with a discussion of a new source of turbulent plasma: the MHD plasma wind tunnel. Some initial results will be presented.

1. Introduction

A turbulent flow refers to the non-linear, fluctuating motion of the fluid elements [1, 2]. More formally, a turbulent fluid has more energy in convective motion than is dissipated as heat. The ratio of those energies is the Reynolds number of the flow given by

$$R_e = \frac{vL}{\nu}$$

where v is a characteristic flow speed, L is a characteristic length of the large-scale flow and ν is the kinematic viscosity. A turbulent fluid has a large Reynolds number, which is to say convection dominates momentum diffusion, and there is a large separation of scales between the convective motion of the fluid and the scale at which the kinetic energy is dissipated as heat. Turbulent flows are characterized by an energy cascade in which energy contained in the largest convective motion of the fluid is transferred via non-linearities to ever smaller scales until it is dissipated. The range between the energy injection scale and the dissipation scale is known as the inertial range.

Fluctuation energy at different scales is represented in Fourier space as a wavenumber power spectrum, $E(k)$. The picture of the energy cascade begins with energy injected at the largest scales (smallest k) by stirring or interaction with boundaries. Non-linearities couple energy to smaller scales

(larger spatial frequency k). In the inertial range, the only process at play is the transfer of energy from one wavenumber k to the next at a rate ϵ. According to an hypothesis by Kolmogorov [3] (see below), the form of the wavenumber spectrum in the inertial range is

$$E(k) = C\epsilon^{2/3}k^{-5/3}.$$

Turbulence in magnetized plasmas is further complicated by magnetic diffusivity characterized by a second Reynolds number:

$$R_m = \frac{\mu_0 v L}{\eta},$$

where η is a resistivity (typically Spitzer). Energy in turbulent magnetoplasmas can be dissipated by either viscosity or resistivity. Places in the fluid where there are sheared flows (vorticity) give rise to viscous dissipation. Places in the fluid where there are sheared magnetic fields (currents) give rise to resistive dissipation. The ratio of these two effects is given by the magnetic Prandtl number:

$$Pr = \frac{R_m}{R_e} = \frac{\mu_0 \nu}{\eta}.$$

Plasmas can be dominated by either viscous or resistive dissipation. In the plasma wind tunnel described below, viscous and resistive dissipation are the same order and the magnetic Prandtl number is near unity.

Another theoretical difficulty is that since $\nabla \cdot \boldsymbol{B} = 0$ (identically), magnetic field lines thread the turbulent volume and are continually wrapped and twisted by the flow. In the limit of very small magnetic diffusivity η/μ_0 the turbulence can amplify the magnetic field at small scales; a turbulent dynamo. It is a topic of ongoing research to see if magnetic energy at small scales can be converted to magnetic flux at large scales.

Three symmetries are important in descriptions of turbulence. Turbulence is called *stationary* if mean values, say $\langle b^2 \rangle$ are independent of the time over which the means are taken. Turbulence is called *homogeneous* if mean values are independent of position (e.g. if $\langle b(r)^2 \rangle = \langle b(r + \Delta r)^2 \rangle$). Finally, turbulence is called *isotropic* if mean values of independent of direction (e.g. if $\langle b_x^2 \rangle = \langle b_y^2 \rangle$). Turbulence never absolutely reflects these symmetries, for example the flow direction away from the Sun is special in the solar wind. We find that for the plasma wind tunnel described below, there are extended periods during which the turbulence is approximately stationary, homogeneous and isotropic. The ergodic theorem states that time averages are the same as ensemble averages, assuming the fluctuations are stationary. We typically perform time averages over short epochs in the plasma wind tunnel (discussed below), but also then perform averages over an ensemble of perhaps 80 realizations.

1.1. Kolmogorov 1941 theory

It is well established that the Navier–Stokes equation

$$\frac{\partial \boldsymbol{v}}{\partial t} + \boldsymbol{v} \cdot \nabla \boldsymbol{v} = -\frac{\nabla P}{\rho} + \nu \nabla^2 \boldsymbol{v}$$

governs incompressible flow, including turbulent flow, but there is no deductive rigorous proof of turbulent flow from the Navier–Stokes equation. Nonetheless, it is clear that turbulence is described by the Navier–Stokes equation (by numerical simulation, for example) and the key criterion for turbulence, the Reynolds number, is derived from the ratio of the convective term (second on the left) to the dissipative term (second on the right).

For fluid turbulence, the energy transfer rate is the kinetic energy (per unit mass) divided by a characteristic time. The characteristic time is the length scale of interest L divided by the velocity itself, so the units of the energy transfer rate are $\epsilon \propto L^2/t^3$. The units of kinematic viscosity are those of a diffusivity $\nu \propto L^2/t$. If one assumes that dissipation occurs at a scale determined only by the energy transfer rate and viscosity (one of Kolmogorov's hypotheses in his 1941 paper), we can identify by dimensional analysis the Kolmogorov dissipation scale,

$$\ell_{\mathrm{K}} = \left(\frac{\nu^3}{\epsilon}\right)^{1/4}.$$

The Kolmogorov scale represents the demarcation point between the inertial range and the beginning of the dissipation range. There is a similar scale associated with magnetic diffusivity, η/μ_0. Note that for small dissipation and large energy transfer rate, the Kolmogorov scale becomes small. The separation between the largest (integral) scale of the turbulence L and the Kolmogorov scale is a function of the Reynolds number: $L/\ell_{\mathrm{K}} = R_e^{3/4}$,

The essence of the Kolmogorov 1941 scaling argument for the omni-directional wavenumber spectrum for fully developed turbulence is that $E(k)$ in the inertial range depends only on k (via a power law) and the energy transfer rate ϵ. This is another of Kolmogorov's hypotheses. Kolmogorov thought about an energy rate per unit mass: $\epsilon \sim v^2/\tau$. For magnetic turbulence, it is magnetic energy, b^2, that is transferred from one scale $L \propto 1/k$ to the next in a characteristic time τ. So the magnetic energy transfer rate is $\epsilon \sim b^2/\tau$, where b is the fluctuating part of the magnetic field, and τ is the time scale over which the energy is transferred.

The dimensions of $E(k)$ are such that

$$\int E(k)\,\mathrm{d}k = \langle b^2 \rangle,$$

so $E(k) \propto b^2/k$. The time τ in the energy transfer rate depends on the physics of the transfer. For MHD, we consider an Alfvén crossing time at the scale L:

$$\tau_{\mathrm{MHD}} = \frac{L}{v_{\mathrm{A}}} \sim \frac{1}{kb}.$$

This is because $\omega_{\mathrm{MHD}} = k v_{\mathrm{A}}$. So now we do dimensional analysis:

$$E(k, \epsilon) = C k^{\alpha} \epsilon^{\beta},$$

$$\frac{b^2}{k} = C k^{\alpha} \left(\frac{b^2}{\tau_{\mathrm{MHD}}}\right)^{\beta} = C k^{\alpha} b^{2\beta} (kb)^{\beta}.$$

We find that $2 = 3\beta$ or $\beta = 2/3$ and $-1 = \alpha + \beta$ so $\alpha = -5/3$. We get the famous Kolmogorov 1941 result:

$$E(k) = Ck^{-5/3}\epsilon^{2/3}.$$

An interesting twist happens if the time scale for the transfer is faster, say due to Whistler waves or kinetic Alfvén waves. In that case, there is a different dispersion relation. We get that $\omega_{\rm Hall} = k^2\delta_i v_{\rm A} = k^2\delta_e^2\omega_{\rm ce}$, or essentially,

$$\tau_{\rm Hall} \sim \frac{1}{k^2 b}.$$

That extra factor of k changes the scaling for $E(k)$ at scales smaller than δ_i.

$$E(k,\epsilon) = C_H k^\alpha \epsilon^\beta,$$

$$\frac{b^2}{k} = C_H k^\alpha \left(\frac{b^2}{\tau_{\rm Hall}}\right)^\beta = C_H k^\alpha b^{2\beta}(k^2 b)^\beta.$$

We find that $2 = 3\beta$ or $\beta = 2/3$ and $-1 = \alpha + 2\beta$ so $\alpha = -7/3$. We get a modified energy spectrum (with a different constant C_H):

$$E_{\rm Hall}(k) = C_H k^{-7/3}\epsilon^{2/3}.$$

1.2. Solar wind

The solar wind is often referred to as the best studied turbulence laboratory (see [4–7] for a set of excellent reviews). Indeed, there are extended periods (hours to days) in which the solar wind is highly stationary. Aside from boundaries at planetary magnetospheres and the heliopause, there are no walls constraining the solar wind. Measurements in the solar wind require expensive spacecraft and seldom are there more than a few spacecraft present to coordinate measurements (the Cluster group uses four satellites in a tetrahedral arrangement). It is known that the solar wind is anisotropic with different statistical character parallel and perpendicular to the local mean field. Magnetic field fluctuations in the solar wind tend to have minimum variance in the direction of the mean magnetic field. Much is known about the turbulence properties of the solar wind. Only a brief overview is presented here.

The solar wind is a high velocity (400 km s^{-1}), low density (10 cm^{-3}) hydrogen plasma with imbedded magnetic field (typically $B \cong 10$ nT $= 100\,\mu$G at 1 AU). The turbulent properties of the solar wind have been studied in great detail near Earth (1 AU) but some satellites (notably Voyagers 1 and 2) have made plasma measurements out to the heliopause, about 120 AU from the Sun. The flow is supersonic and super-Alfvénic (with M about 10), and there are periods of fast wind with velocities over 600 km s^{-1}. Temperatures in the solar wind plasma are typically about 10 eV with $T_{\rm i} \geqslant T_{\rm e}$. Plasma beta ($\beta = W_{\rm th}/W_{\rm B}$), again at 1 AU, is approximately unity, indicating that neither magnetic pressure nor kinetic pressure dominates the dynamics. Interestingly, the solar wind is essentially collisionless; the mean free path for inter-particle collisions is approximately 1 AU. Nonetheless, the solar wind behaves in many ways like a collisional conventional fluid, with interactions mediated via waves.

The solar wind is the only astrophysical collisionless plasma that we can study *in situ*. It is clear that the solar wind exhibits fully developed turbulence in the sense that an active cascade is present in all dynamical MHD quantities (B, v, n) as we will show in section 2. The fluctuations tend to be Alfvénic insofar as $\boldsymbol{B}$ and $\boldsymbol{v}$ are either aligned or anti-aligned at large scales. Solar wind turbulence contains coherent structures that reveal themselves as temporal intermittencies in the flow. Since the solar wind plasma is effectively collisionless (the collisional mean free path is on the order of one AU), the wave processes that mediate the turbulent evolution create anisotropies at the smallest scales.

As we will discuss in section 2, turbulent dynamics can be studied in both the time domain and space domain. Analysis of solar wind plasma has focused on the time domain since typically only single spacecraft are available (with some exceptions) and the Taylor hypothesis is invoked ($f = V_{\rm SW}/\lambda$, discussed below). The turbulent cascade is manifest through the frequency power spectrum. Coherent structures and intermittency is manifest in non-Gaussian features in the probability distribution function of temporal increments.

1.3. Fusion devices

The most studied turbulent laboratory plasmas have been toroidal magnetic confinement fusion devices such as tokamaks and reversed field pinches [8, 9]. There have been several excellent reviews on magnetic turbulence in tokamaks [10], electrostatic edge turbulence in tokamaks [11], and comparisons of the two [12]. In low β magnetic confinement fusion devices, electrostatic fluctuations should dominate (especially in the edge). Because of this, much more is known about electrostatic edge turbulence than magnetic fluctuations. Nonetheless, magnetic fluctuation studies in laboratory plasmas have primarily been studied in devices designed for magnetic confinement fusion. There have been very few laboratory studies of MHD turbulence in laboratory plasmas in non-fusion devices. This provides the motivation for the Swarthmore Spheromak Experiment (SSX) MHD wind tunnel described in section 4.

The transport of heat and particles in magnetic confinement fusion devices exceeds that due to inter-particle collisions by a large factor. In the core of these devices, magnetic fluctuations are implicated ($\delta B/B$) [13], while in the edge the turbulence is largely electrostatic drift waves ($\delta n/n$) [14]. The sources of free energy are radial gradients in density and temperature. In any case, *in situ* measurements of these fluctuations are difficult in modern fusion devices [15]. Since magnetic fluctuations dominate in the core, measurements of $\delta B/B$ have been particularly challenging.

The simple picture of transport from magnetic fluctuations is due to Rechester and Rosenbluth presented in a classic paper [13]. The idea is that turbulence causes a perturbation in the equilibrium magnetic field of the plasma δB_r. Particles that are normally on confined orbits effectively experience a diffusive step Δr of order $\delta B_r/B_0$, so that diffusion ($D \sim (\Delta r)^2/\tau$)

scales like $(\delta B_r/B_0)^2$. The Rechester–Rosenbluth diffusion coefficient for electron transport becomes approximately

$$D \sim \left(\frac{\delta B_r}{B_0}\right)^2 v_e L_\parallel,$$

where v_e is the electron thermal speed and $L_\parallel$ is the correlation length along the field line. The energy confinement time in tokamaks has been shown to depend on the magnetic Reynolds number (and β) indicating that MHD turbulence plays a role in confinement [10].

Electrostatic turbulence in laboratory plasmas is an active area of research and will only be touched on here. Density gradients in magnetized plasmas can destabilize drift waves. Strong drift wave turbulence has been implicated in degraded confinement in tokamaks (so-called L-mode), and $E \times B$ velocity shear at the edge (from a radial E_r) has been shown to mitigate turbulence and increase confinement [16, 17]. The sheared $E \times B$ flow breaks up turbulent eddies at the edge forming a transport barrier. Much is known about the turbulent character of the density fluctuations in drift wave turbulence. Among other things, it has been shown that the frequency power spectrum for density fluctuations $\delta n/n$ have a similar character in a range of magnetic confinement fusion devices [11], typically with a very steep spectral index ($\alpha \geqslant 3$).

The subject of turbulent or anomalous transport in magnetic confinement fusion devices is vast, so we will focus on turbulence measurements in a few cases. The emphasis in the fusion community has been on turbulent transport but our emphasis here will be on the types of statistical turbulent measures discussed below. In section 3, we will focus our review on early measurements of magnetic turbulence in the Zeta reversed field pinch [18], later measurements of fluctuations in a tokamak [9], and recent measurements of the spatial magnetic fluctuation spectrum in the MST reversed field pinch [19, 20].

2. Overview of statistical tools for turbulence

Here we review the types of measurements and analytical tools used in the study of fully developed turbulence. These are described in much more detail in Batchelor [1] and Frisch [2], and have been largely developed in the study of turbulence in air in conventional wind tunnels and water in tidal channels [21]. These tools can be applied to scalar fields such as density n and temperature T, as well as vector fields such as velocity $\boldsymbol{v}$ and magnetic field $\boldsymbol{b}$. We will focus on the magnetic field here.

A suitable turbulent laboratory plasma source should admit the use of these tools. In other words, there should be a means to make several simultaneous measurements at multiple locations, and the turbulent plasma should persist for several dynamical times. The time cadence of the measurement should be high enough to resolve physics of interest (for example, oscillations at the proton cyclotron frequency). In addition, the spatial separation of detectors should resolve at least the spatial correlation length of the turbulence (defined below).

In figure 1 we show a sample dataset from the SSX plasma wind tunnel. In this case, magnetic field is measured at 4 mm resolution (close to the proton gyroscale). Evidently, spatial resolution is satisfactory since signals from adjacent locations are very similar, while signals from distant locations are dissimilar. This observation gives a crude estimate of the spatial correlation length. These records consist of over 2500 time steps. Long records should be available for the computation of higher order statistics such as structure functions. The types of tools naturally divide into time domain and space domain. In each case, we will present an example of the technique from either a solar wind or laboratory plasma measurement, or from a numerical simulation.

2.1. Time domain

Time domain analysis begins with a time series of a fluctuating quantity, for example a component of the magnetic field $\boldsymbol{b}(t)$ (see figure 1). If the spatial resolution is good, time series from a few spatial locations can be averaged together. For the SSX plasma wind tunnel data presented later, we consider the signal from a single magnetic probe. In a typical experimental plasma discharge, there will be different stages during its evolution (start-up, steady state, decay), and the character of the turbulence is different at each stage. We will generally select an epoch of interest for study during a suitable period rather than analyzing the entire record. In addition, the epoch of interest should be during a period of otherwise stationary turbulence. By stationary we mean that average values are independent of the choice of time origin. Finally, the time series should persist for several dynamical times, in this case, several Alfvén times $t_A = L/v_A$, where the Alfvén speed is the characteristic velocity in a magnetized plasma: $v_A = B/\sqrt{\mu_0 M n}$, where B is the local magnetic field, M is the ion mass and n is the number density. Four important temporal statistical tools of turbulence for time series are described below.

2.1.1. Autocorrelation function. It is useful to measure the correlation time of the turbulence, i.e. the time it takes a time series to 'lose its memory' or become de-correlated. Visual inspection of figure 1 shows that the waveform is self-similar at around 1 μs or less, but clearly different at separations of 10 μs or more. To determine the correlation time of the signal, we multiply the time series by a copy of itself and introduce a time lag:

$$R(\tau) = \langle \boldsymbol{b}(t+\tau)\boldsymbol{b}(t)\rangle.$$

The autocorrelation function is often normalized to unity by dividing by $\langle \boldsymbol{b}(t)\boldsymbol{b}(t)\rangle$. Strictly speaking, R_{ij} is a tensor if we consider correlations of different components of $\boldsymbol{b}$, but we will focus on single components (the diagonal elements of the tensor). Functionally, we compute the correlation coefficient for a particular τ by averaging over a time interval during a stationary phase of the turbulence, then averaging this result over several realizations of an ensemble. If the turbulence is truly stationary, then the function $R(\tau)$ should be independent of the choice of the origin of t. This is a good functional check of stationarity. Correlation coefficients are computed in this way for a range of τ's in order to construct $R(\tau)$. We have

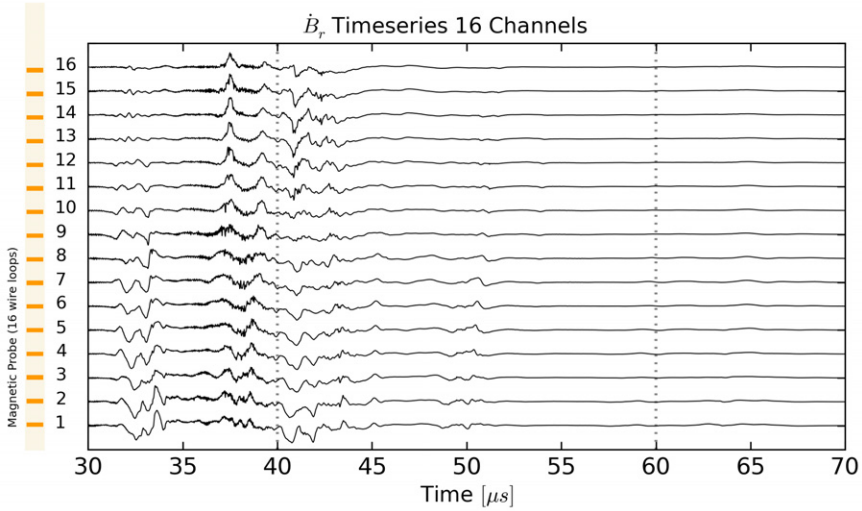

Figure 1. Array of waveforms. A sample array of waveforms from the SSX MHD wind tunnel. Satisfactory spatial resolution is evident from the similarity of adjacent waveforms. Data displayed is 14-bit and recorded at 65 MHz.

in mind studying a single component of the magnetic field $\boldsymbol{b}(t)$, but one could study correlations of the scalar product $\boldsymbol{b}(t+\tau)\cdot\boldsymbol{b}(t)$. $R(\tau)$ is an even function, i.e. $R(+\tau) = R(-\tau)$. We define the de-correlation time τ_C as the time at which $R(\tau)$ drops by some factor: $1/2$ or e^{-1}. A more general definition involving the normalized function is $\tau_C = \int R(\tau)\,\mathrm{d}\tau$. Later, when we perform time averages, we demand that averages are taken over many de-correlation times. The stationary phase of the turbulence should persist for many de-correlation times.

The autocorrelation function in the solar wind has been measured several times. The notion of stationarity in the solar wind (i.e. that average properties of $\mathbf{B}(t)$ do not depend on the origin of time) has also been tested. In a classic set of papers, Matthaeus and Goldstein [22] analyzed magnetometer data from Voyager, ISEE 3 and IMP satellites, and found correlation times in the range 50 000 s, but can be an order of magnitude smaller or larger depending on solar wind speed and other parameters. They also found that the solar wind magnetic field is statistically time stationary, at least in the 'weak' sense. Weak stationarity suggests that the simple two-time $R(\tau)$ defined above ($N = 2$) should be independent of the choice of the origin of t, while strict stationarity requires that all higher order correlations ($N \geqslant 2$) are independent of time origin. Examples of $R(\tau)$ appear in Matthaeus and Goldstein, figure 1 [22] and figure 10 [22]. Many other interesting statistical measures are presented in these papers.

In figure 2 we show an example of a temporal autocorrelation function from the SSX wind tunnel. Autocorrelation from all three components of the magnetic field from a single location are shown. Note that as we see from visual inspection of figure 1, the autocorrelation time is on the order of 1 μs, and fluctuations rapidly de-correlate for times larger than that.

2.1.2. Frequency power spectrum $E_B(f)$. The spectral content of the time series $b(t)$ can be obtained with a Fourier transform or wavelet transform. Typically, we deal with the

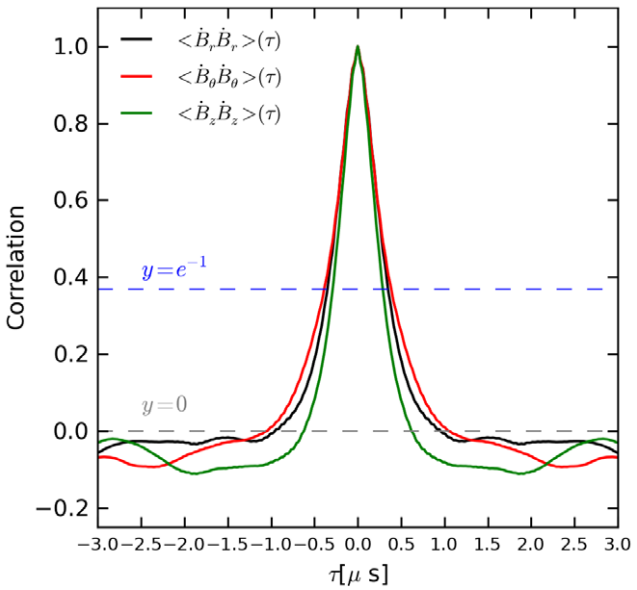

Figure 2. Autocorrelation function. A sample autocorrelation function from the SSX MHD wind tunnel. Shown here is the temporal autocorrelation function for all three components of B at a single spatial location. The autocorrelation time is on the order of 1 μs.

purely real power spectrum $E_B(f)$ or $E_B(\omega)$:

$$E_B(\omega) = \frac{1}{T}\left[\int_0^T b(t)\mathrm{e}^{-\mathrm{i}\omega t}\,\mathrm{d}t\right]^2,$$

where $\omega = 2\pi f$. If the turbulence is homogeneous, we should find the same spectrum for $b(t)$ anywhere in the plasma. If the turbulence is isotropic, we should find the same spectrum for any component of $\boldsymbol{b}(t)$. In a turbulent flow, the frequency power spectrum is most useful if spatial structures are frozen into the flow. This is the Taylor hypothesis [23], meaning that if a structure of size δ is convected by a probe at velocity V, then a frequency of order $f = V/\delta$ is registered in the power

spectrum. In this way, information on spatial fluctuations is encoded in the time series (i.e. time derivatives can be converted to spatial derivatives). The hypothesis pertains as long as the magnetic field of the structure changes slowly during the time the structure is advected across the probe. Another way to state it is that the fluctuation velocity v in the moving plasma frame is small, $v/V \ll 1$. This is a good assumption for high flow speeds and small structures. It is an especially important assumption in the turbulent analysis of the solar wind.

An excellent example of a frequency power spectrum from the solar wind was discussed by Sahraohi *et al* [24]. In this measurement, very high frequency (100 Hz) solar wind magnetic and electric data were analyzed from the Cluster spacecraft. Data from a 3 h epoch were studied. During this time, the solar wind speed was 640 km s^{-1} so at 100 Hz, structures as small as 6.4 km could be detected. The plasma density was $n \sim 3\,\mathrm{cm}^{-3}$ and the mean magnetic field was $B \sim 6$ nT. At that density, $\delta_i = c/\omega_{\mathrm{pi}} \sim 130$ km. The plasma temperatures were $T_{\mathrm{p}} \sim 50$ eV and $T_{\mathrm{e}} \sim 12$ eV, so the proton gyroradius was $\rho_{\mathrm{i}} \sim 120$ km and the local proton gyrofrequency is $f_{\mathrm{cp}} \sim 0.1$ Hz.

In figure 3, the frequency power spectrum (in units nT^2 Hz^{-1}) is presented. Low frequency data (below about 1 Hz) is from the flux gate magnetometer (FGM), while higher frequency data are from the Cluster STAFF search coil (SC). The data are resolved into fluctuations parallel and perpendicular to the mean magnetic field. There is more energy in the perpendicular fluctuations so the turbulence is anisotropic, but the slopes are similar indicating that during this 3 h epoch, the anisotropy seems to be independent of scale. The low frequency part of the spectrum is consistent with the Kolmogorov prediction of $k^{-5/3}$, again assuming the Taylor hypothesis so $\omega = kV$. The key point of the figure is that is that there are two break points in the spectrum, and the breakpoints are associated with structures advected across the satellite at solar wind speed and not with characteristic frequencies in the plasma frame. In other words, because the wind velocity is so high ($V \gg v_{\mathrm{tp}}$), the frequency $f_{\rho\mathrm{p}} = V/\rho_{\mathrm{p}}$ is much higher than the proton gyrofrequency $f_{\mathrm{cp}} \sim v_{\mathrm{tp}}/\rho_{\mathrm{p}}$ and much more consistent with the measured break point in the spectrum.

The standard tool for computing the frequency power spectrum is the fast Fourier transform or FFT. The FFT affords an improvement in computational speed of the discrete Fourier transform from $\mathcal{O}N^2$ to $\mathcal{O}N\ln N$ (hence 'fast'). Typically, however, the FFT is taken over a long time duration, often the entire record. It is often useful to analyze the spectrum as a function of time. This can be accomplished with a windowed FFT. Some groups have adopted the more flexible wavelet transformation [25]. The idea of the wavelet transform is to isolate shorter portions of the waveform for analysis while providing some weight to the entire time series. The time localization and weighting is performed by selection of the 'mother wavelet'. We consider three typical mother wavelets below (derivative of Gaussian or DoG, Paul and Morlet).

We present three figures (figures 4, 5 and 6) which show the wavelet decomposition of a single $\dot{B}_\theta$ time series from a single shot of the SSX MHD plasma wind tunnel for three

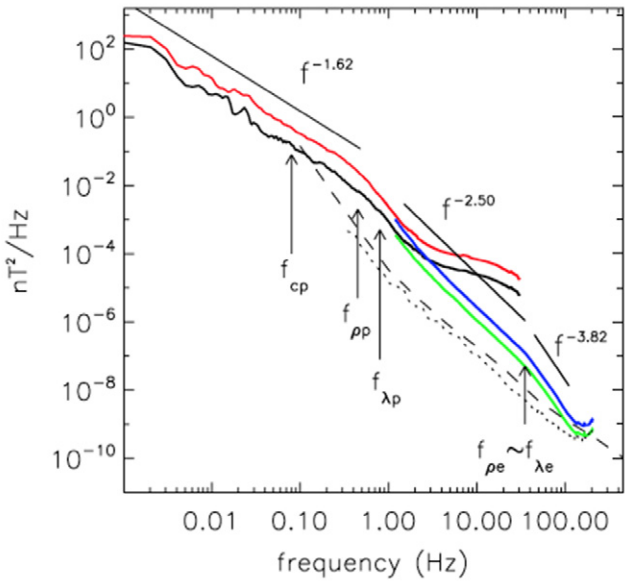

Figure 3. Frequency power spectrum. The parallel (black) and perpendicular (red) frequency power spectrum measured in the solar wind with the Cluster satellite. Note the $-5/3$ index in the inertial range, followed by a steeper index in the dissipation range at higher frequencies [24].

different mother wavelets (DoG, Paul and Morlet). Each plot has the full wavelet spectrum in frequency and time space in subplot (c). Subplot (a) for each figure has the total summed spectra power over the entire time range and compared to an FFT computed over that same range. Subplot (b) has the total power summed over the frequencies indicated in the legend for each time step. Subplot (d) shows the original time series data. The key point of subplot (a) is that each wavelet clearly captures the essential features of the FFT, while enabling the possibility of more localized time analysis. The wavelet approach has other advantages.

Comparison amongst the three plots highlights the advantages and disadvantages of each particular mother wavelet. Morlet tends to have the highest resolution in frequency space. Note that the total spectrum in subplot (a) has the most wiggles. However, the time resolution of the Morlet is the poorest and as such as the smoothest curve in subplot (b). The Morlet wavelet also matches up best to Fourier scales so the red and orange curves in subplot (a) line up the closest. Conversely, the Mexican-hat mother wavelet or derivative of Gaussian, $n = 2$, has the worst frequency resolution, but best temporal resolution. The correspondence between wavelet scales and Fourier scales for DoG is not as good and so the red and orange curves do not match up as well (nor does the wavelet probe as high a frequency). The Paul wavelet is a good intermediate between the two. The use of the Morlet wavelet in the analysis mainly comes out of its good frequency resolution and correspondence to Fourier scales.

Finally, there is a mathematical connection between the previously discussed correlation function and the power spectrum. The Weiner–Khinchin theorem states that the autocorrelation function and the frequency power spectrum

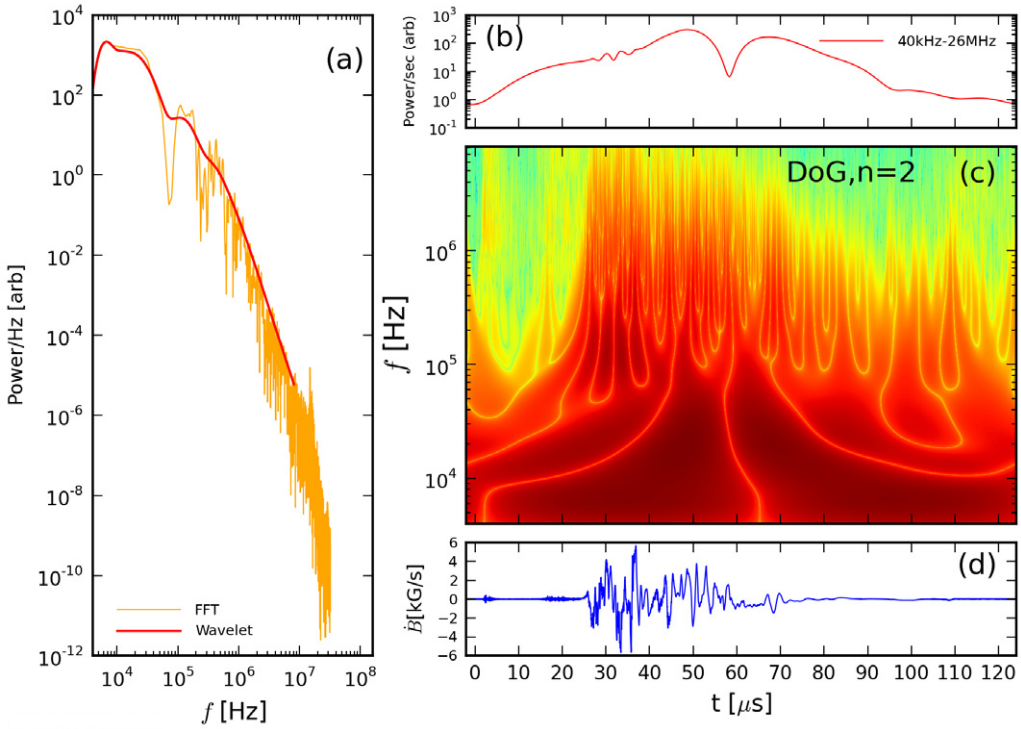

Figure 4. DoG wavelet, $n = 2$: (a) spectrum, (b) total power, (c) full wavelet spectrum in time and frequency space, (d) raw waveform data.

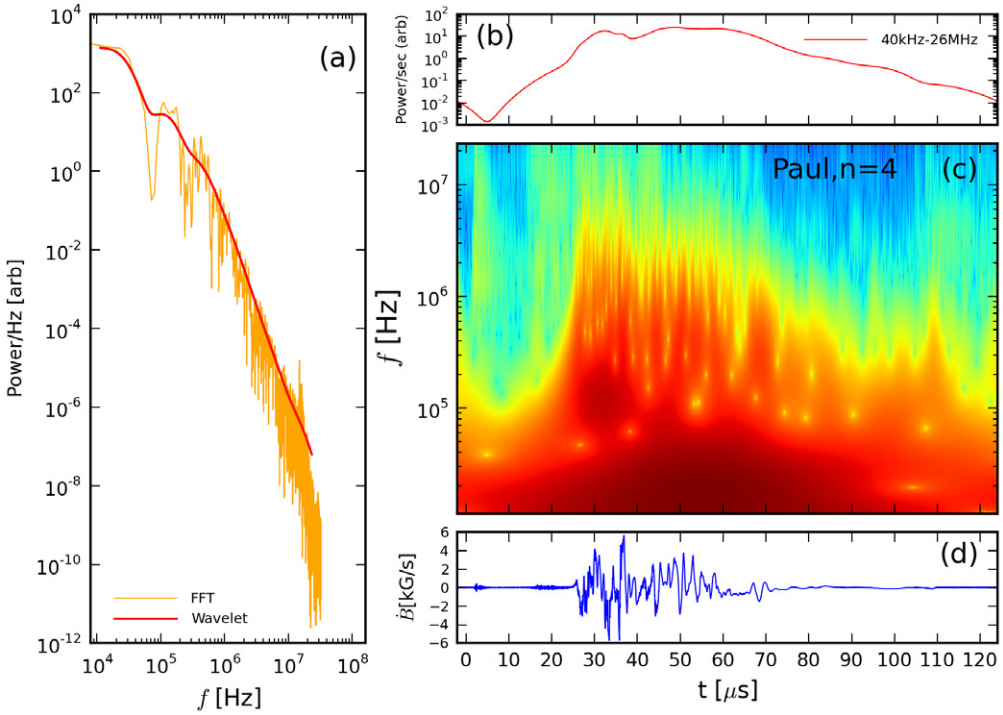

Figure 5. Paul wavelet, $n = 4$: (a) spectrum, (b) total power, (c) full wavelet spectrum in time and frequency space, (d) raw waveform data.

form a Fourier transform pair:

$$E_B(\omega) = \frac{1}{2\pi}\int_{-\infty}^{+\infty} R(\tau)\mathrm{e}^{\mathrm{i}\omega\tau}\,\mathrm{d}\tau.$$

This relationship is sometimes useful if one has high quality correlation function data and wishes to study the power spectrum, for example.

2.1.3. Temporal increment. In order to detect the presence of coherent structures in a time series, one can employ the technique of temporal increments [26–29]. If the fluctuations in a stationary time series are truly random, then after some delay τ (beginning at any time t in the time series), we expect as many upward changes in the signal as downward changes, and we expect large increments to be rare. This can be quantified

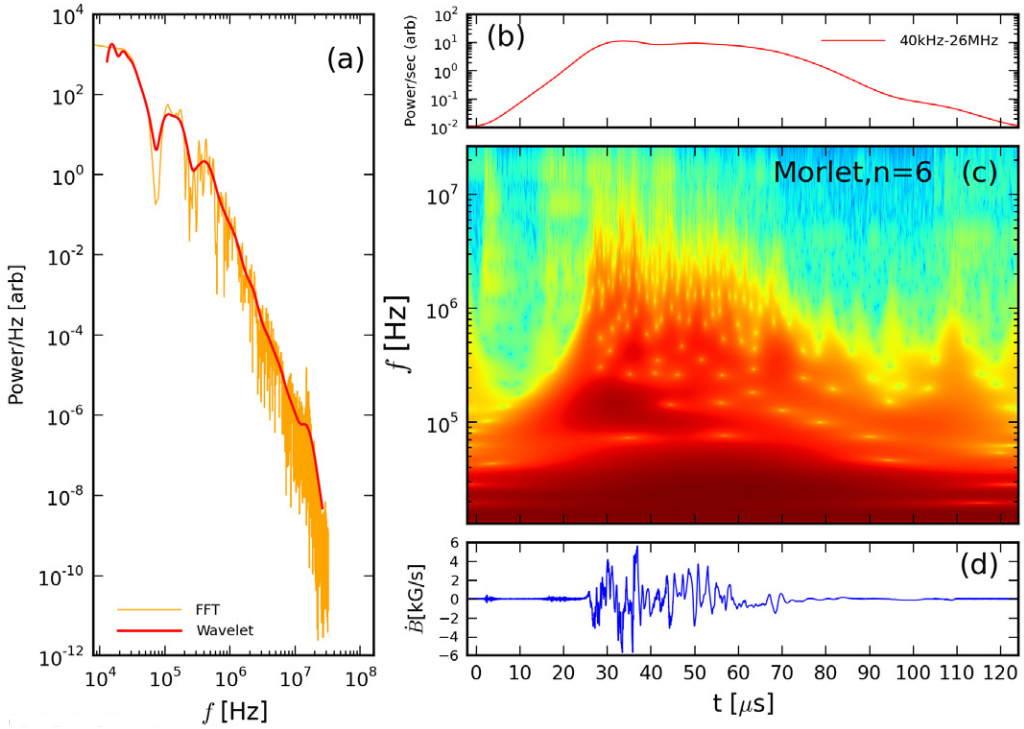

Figure 6. Morlet wavelet, $n = 6$: (a) spectrum, (b) total power, (c) full wavelet spectrum in time and frequency space, (d) raw waveform data.

by constructing a record of increments for some time lag τ:

$$\Delta \boldsymbol{b} = \boldsymbol{b}(t + \tau) - \boldsymbol{b}(t),$$

then studying the probability density function (PDF) of the record. Regions of high magnetic stress in the flow will be reflected in rapid changes, large excursions, or even discontinuities in the increment. The PDF of increments will have a mean value (typically near zero for steady or stationary turbulence) and a variance σ^2. The PDF of increments can be compared with a Gaussian with the same mean and variance. It is often observed, for example in the solar wind [28, 29], that PDFs of increments are much broader than expected from a Gaussian or normal distribution. These 'fat tails' can be quantified using the statistical metric flatness (or kurtosis) for each time lag τ: $F(\tau) = \langle \Delta b^4 \rangle / \langle \Delta b^2 \rangle^2$. A Gaussian distribution has $F = 3$ but turbulent PDFs of increments can have a flatness an order of magnitude higher.

As an example of this technique, we consider a solar wind measurement and simulation comparison by Greco *et al* [29]. A 27-day time series of magnetic data was studied from the magnetic field experiment on the ACE spacecraft. The data were subdivided into 12 h subintervals, and increments $\Delta \mathbf{b}$ were computed for $\tau = 4$ min, normalized to the standard deviation for each 12 h subinterval. PDFs of increments were constructed and compared to unit variance Gaussians.

In figure 7, the PDFs of normalized increments of one component of magnetic field from ACE data are plotted along with PDFs from both 2D and 3D MHD simulation data. The key result is that the 2D simulation more closely matches the ACE solar wind data; both have non-Gaussian 'fat tails' suggestive of a preponderance of small-scale coherent

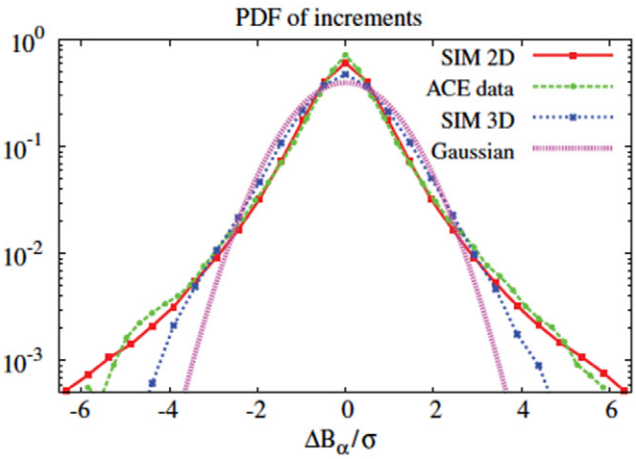

Figure 7. Temporal increment. PDFs of the normalized temporal increment comparing ACE satellite data with both 2D and 3D simulations [29]. Reprinted with permission.

structures. A close analysis of the 2D simulation shows what kind of structure contributes to the non-Gaussian tails and the culprit is a sea of small-scale current-sheet-like structures that form the sharp boundaries between magnetic flux tubes.

Further studies have associated ion heating with the 'spontaneous cellularization' of solar wind turbulence [30, 31]. The idea is that as MHD turbulence evolves, flux tubes, discontinuities, and thin current sheets form as part of the temporal evolution and relaxation processes. The discontinuities and current sheets, revealed by the PDF of increment technique described here, can become sites of local plasma heating if magnetic reconnection ensues.

2.1.4. Temporal structure function. Averages of powers of increments are called structure functions.

$$S_B^p(\tau) = \langle (\boldsymbol{b}(t+\tau) - \boldsymbol{b}(t))^p \rangle.$$

Functionally, we generate a table of increments for some time lag τ. These are all raised to the power p, and we compute the average. Again, the average is first over a short time duration during the stationary phase of turbulence for each discharge, then an ensemble average is performed over several realizations. The process is repeated for a series of τ's. Alternatively, the PDF of increments can be constructed for a range of time lags τ and the p^{th} moment can be taken. Note that structure functions have already been utilized above in computing the flatness. Flatness can be viewed as fourth-order structure function suitably normalized.

Temporal structure functions have been studied in the solar wind (see the review by Marsch and Tu [32] and references therein, as well as [33]) and the ionosphere [34]. Assuming again the Taylor hypothesis that the rate of evolution in the plasma frame is slow compared with the rate at which structures are advected by spacecraft, the prediction from Kolmogorov turbulence theory is $S^p(\tau) \propto \tau^{p/3}$ [2]. In other words, a log–log plot of $S_B^p(\tau)$ for some power p should have a linear region corresponding to the inertial range. Famously, the second-order structure function grows like $\tau^{2/3}$ in numerous wind tunnel experiments [2]. Growth of the second-order structure function like $\tau^{2/3}$ is closely connected with the frequency power spectrum (another second-order statistical quantity) dropping like $f^{-5/3}$ in Kolmogorov turbulence. Data from long time series from the Voyager and Helios spacecraft show structure functions with slopes much flatter than the Kolmogorov prediction. In the Marsch and Tu review, data from structure functions up to 20^{th} order are shown. It is only above sixth order that departures from the Kolmogorov prediction are observed.

In a recent series of observations using the Cluster spacecraft and the FGM and STAFF-SC instruments discussed above, Kiyani *et al* [33] measured high-order structure functions in a stationary interval of fast solar wind. In figure 8, a log–log plot of $S_B^p(\tau)$ versus τ shows an increase in the slope as the order increases from $p = 1$ to 5. An increase is observed for both the inertial range ($\tau > 10$ s) as well as the dissipation range ($\tau < 1$ s). Just as in the March and Tu review, the Kiyani *et al* results show structure functions with slopes flatter than the Kolmogorov prediction at the higher orders due to intermittency.

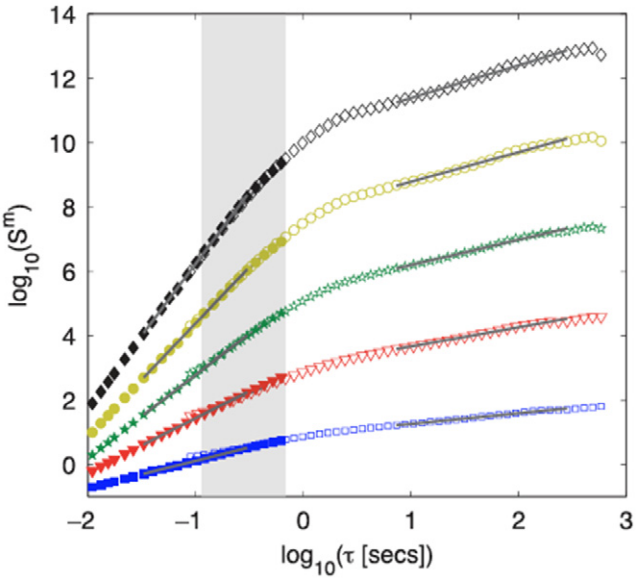

Figure 8. Temporal structure function. Structure functions of order 1 to 5 from magnetic fluctuations measured by the Cluster spacecraft [33]. Reprinted with permission.

2.2. Space domain

Just as with the time domain, we can take either products or differences of snippets of waveforms (see figure 1). In a typical experiment, and certainly in solar wind observations, we have access to long time series but typically sampled at many fewer spatial locations than time points. As such, space domain metrics are often computed over some brief time period, though at least a few de-correlation times. Products of nearby waveforms yield a finite number; a correlation coefficient of unity if properly normalized. Distant waveforms are uncorrelated so products tend to cancel, and spatial correlation coefficients approach zero. Differences of nearby waveforms cancel, so structure functions begin at zero. Distant waveforms are uncorrelated so differences yield a finite number, and structure functions grow with separation. The following are four spatial turbulence metrics analogous to the temporal metrics just discussed.

2.2.1. Spatial correlation function. The analog of the autocorrelation function is the spatial correlation function

$$R(r) = \langle \boldsymbol{b}(x+r)\boldsymbol{b}(x) \rangle.$$

Here $\langle ** \rangle$ implies an average over a short temporal epoch (but longer than a temporal de-correlation time) then an average over all realizations in the ensemble. In some instances, particularly in the solar wind, true ensembles are problematic so longer time averages replace ensemble averages, invoking the as-yet unproven ergodic hypothesis. Typically, $R(r)$ is normalized by $\langle \boldsymbol{b}(x)\boldsymbol{b}(x) \rangle$. Functionally, we select a brief time epoch of interest, multiply the two waveforms and average over that epoch. If the turbulence is spatially homogeneous, one can repeat this process for all pairs of detectors separated by the same distance for the same realization. Finally, an ensemble average is performed over many identical realizations. For well-behaved turbulence, the magnetic fluctuations at two points should become uncorrelated at large spatial separation and the correlation function should vanish ($R \to 0$ as $r \to \infty$).

Two-point velocity correlation functions have been measured in conventional fluids for decades (see, for example [35]) but two-point magnetic correlations in plasmas are less common. The first proper two-point single time measurements of the magnetic correlation function in the solar wind plasma were performed by Matthaeus *et al* [36]. They used simultaneous magnetic field data from several spacecraft,

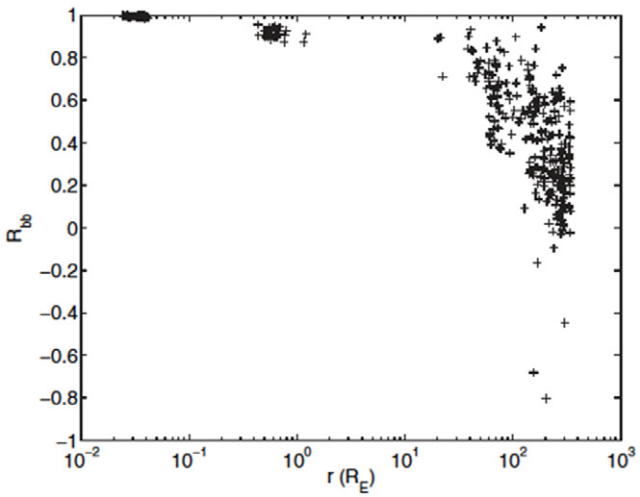

Figure 9. Spatial correlation function. Measured using ACE–Wind data and Cluster data (closer separations). A parabolic fit to $R(r)$ yields the Taylor microscale [36]. Reprinted with permission.

including the four Cluster spacecraft flying in tetrahedral formation. Simultaneous measurements were performed with separations as small as 150 km (using pairs of Cluster satellites) to as large as $350\,R_E$ (2.2×10^6 km). From measurements of the outer correlation scale, and the Taylor microscale (discussed below), they report an effective magnetic Reynolds number of solar wind $R_m^{\rm eff} = 230\,000$.

In figure 9, a magnetic correlation function $R(r)$ for the solar wind is presented. Three sets of multi-spacecraft data are used. First, at relatively small separations of $0.024-0.042\,R_E$ (about 150–270 km), data from the Cluster satellites from 2004 are used. Next, Cluster data at wider separations of $0.4–1.2\,R_E$ (about 2500–7600 km). Finally, correlation coefficients from the ACE–Wind pair of satellites at separations up to $350\,R_E$ are used. From the data in figure 9, the authors were able to estimate the Taylor microscale of the solar wind from the curvature of $R(r)$ near $r = 0$. The Taylor microscale is the scale associated with mean square spatial derivatives of the fluctuating magnetic field b. The magnetic Taylor microscale can be formally defined as

$$\lambda_T^2 = \frac{\langle b^2\rangle}{\langle(\nabla\times b)^2\rangle}.$$

It is at this scale that one would expect dissipation effects, say from reconnecting current sheets, to become important. From the Taylor microscale λ_T and an estimate of the larger correlation scale of the solar wind ($\lambda_{\rm CS} = \int_0^\infty R(r)\,{\rm d}r$), an effective turbulent magnetic Reynold's number can be written [1]:

$$R_m^{\rm eff} = \left(\frac{\lambda_{\rm CS}}{\lambda_T}\right)^2.$$

A large Taylor Reynold's number so-defined ($R_m^{\rm eff} \gg 1$) is often invoked as a true measure of a turbulent flow since $R_m^{\rm eff}$ is independent of arbitrary dimensions (like the size of a device) or a diffusivity based on microphysics or collisions.

2.2.2. Wavenumber power spectrum $E_B(k)$. The spectral content of an array of spatial measurements $b(r)$ can be obtained with a Fourier transform in a way completely analogous with the frequency power spectrum. Typically, we deal with the purely real power spectrum $E_B(k)$:

$$E_B(k) = \frac{1}{R}\left[\int_0^R b(r){\rm e}^{-{\rm i}kr}\,{\rm d}r\right]^2.$$

Operationally, we construct an array of $b(r)$ at a fixed time (or averaged over a short epoch of times), then compute the Fourier transform. The square of the FFT is the power spectrum. Several power spectra can be averaged within a stationary phase of turbulence of a single realization, then spectra from many realizations can be ensemble averaged. True single time wavenumber power spectra are difficult to construct in solar wind plasmas since typically no more than four spacecraft make coordinated simultaneous measurements (Cluster, for example). To our knowledge, there are no single time wavenumber power spectra of the solar wind yet published.

Laboratory experiments, on the other hand, afford the possibility of fielding many detectors for simultaneous measurement. For example, the wavenumber power spectrum $\tilde{B}^2(k)$ has been measured in the MST reversed field pinch [19]. Fluctuations at large scales are measured by a two-point correlation technique allowing access to the 'tearing mode range' (scales greater than about 10 cm or so). Small-scale fluctuations (between 1–10 cm) are measured by a linear array of magnetic probes. Importantly, because of the known magnetic geometry of MST, these fluctuations are easily resolved into perpendicular and parallel components with respect to the applied field ($k_\perp$ and $k_\parallel$). These probes are similar to those used in the MHD wind tunnel discussed below.

In figure 10, true wavenumber power spectra for $k_\perp$ and $k_\parallel$ are plotted. The fluctuations are clearly anisotropic with a much flatter spectrum for plasma waves propagating across the applied magnetic field than along it. This disparity is characteristic of anisotropic MHD turbulence, for example that observed in the solar wind [37]. It is important to note the distinction between spectra corresponding to a wave-vector k and spectra corresponding to fluctuations projected onto a local coordinate, defined by the momentary local magnetic field for example. This latter case is called variance anisotropy. Typically, in the solar wind, power in fluctuations perpendicular to the local magnetic field exceeds power in fluctuations parallel to the local field by less than an order of magnitude (see figure 3). Interestingly, in this laboratory experiment, the anisotropy is three orders of magnitude. The connection between wavenumber anisotropy and variance anisotropy is ambiguous. In other words, a wave mode propagating purely across the applied magnetic field (e.g. a magnetosonic wave) will have variance anisotropy parallel to the local magnetic field.

The MST data presented here reaches into the dissipation range, so the authors perform a fit to a model that includes the characteristic Kolmogorov $k_\perp^{-5/3}$ scaling, as well as an exponential dissipation term:

$$E_B(k) = \epsilon^{2/3}k_\perp^{-5/3}\exp\left(-b(k/k_{\rm d})^\alpha\right).$$

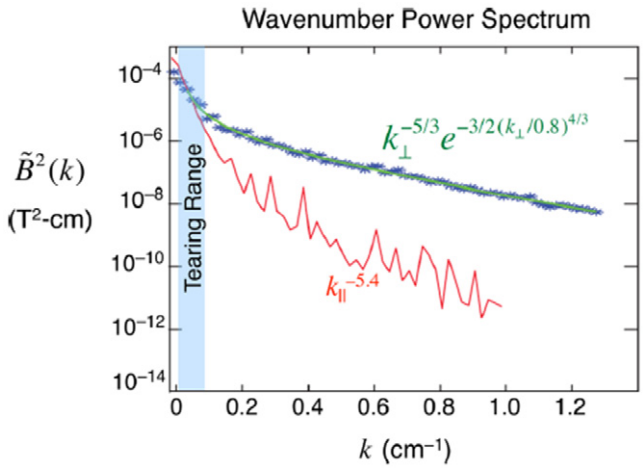

Figure 10. Wavenumber power spectra. Parallel and perpendicular wavenumber power spectra measured in the MST reversed field pinch [19]. Reprinted with permission.

The authors find a dissipation wavenumber $k_\mathrm{d} = 0.6\,\mathrm{cm}^{-1}$, suggesting dissipation at about the ion gyroscale of 1 cm in MST. Values of $\alpha = 4/3$ and $b = 3/2$ are consistent with theoretical models discussed in the paper.

Finally, in complete analogy with the temporal case above, there is a mathematical connection between the spatial correlation function and the wavenumber power spectrum. The Weiner–Khinchin theorem states that the wavenumber power spectrum and the spatial correlation function form a Fourier transform pair:

$$E_B(k) = \frac{1}{2\pi}\int_{-\infty}^{+\infty} R(r)\mathrm{e}^{\mathrm{i}kr}\,\mathrm{d}r.$$

Again, this affords the researcher some flexibility if data is in one form or the other.

2.2.3. Spatial increment. Experimental measurements of true single time spatial increments are much more challenging than temporal increments since typically, many fewer spatial locations are sampled in an experiment than temporal points. This is particularly true in the solar wind. Perhaps the best examples of spatial increment studies come from MHD simulations [28, 29, 38]. The spatial increment is defined in complete analogy with the temporal increment discussed above:

$$\Delta\boldsymbol{b} = \boldsymbol{b}(s + \Delta s) - \boldsymbol{b}(s),$$

where s is some (perhaps 3D) trajectory and Δs is a spatial separation or lag along the path. We have in mind a component of $\boldsymbol{b}$, but strictly speaking one can project the vector increment on the direction Δs.

Servidio *et al* [38] ran a 2D turbulent MHD simulation (4096^2 grid points) and stopped the run at 0.4 Alfvén times when the turbulence was fully developed. They then selected a path s through the data set and computed the spatial increments along the path. A small spatial lag was chosen, $\Delta s = 0.67\lambda_\mathrm{d}$ where λ_d is the dissipation scale for the simulation. For the purposes of the study, they constructed a related metric called the partial variance of increments (PVI) [28, 29]:

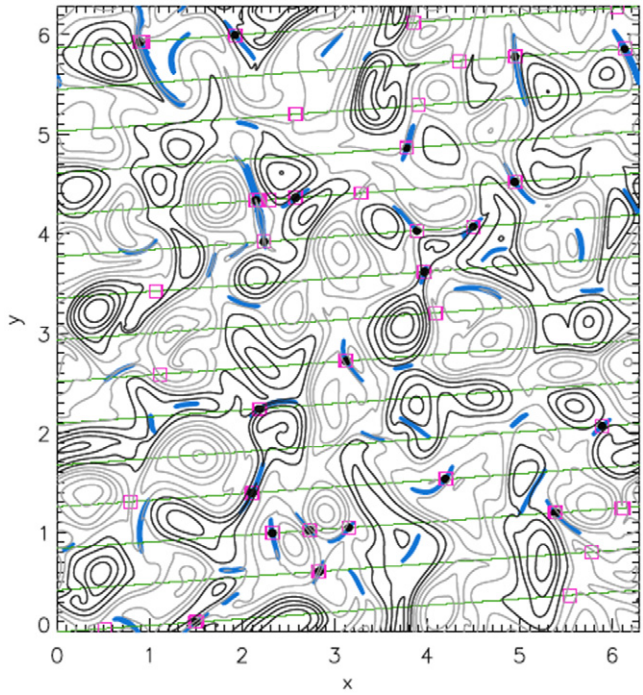

Figure 11. Spatial increment. Contour lines of magnetic field from a 2D MHD simulation. A sample trajectory (green) passes through discontinuities that may be associated with active current sheets (blue). Note that not all large increments (magneta) are also current sheets [38]. Reprinted with permission.

$$\mathcal{I}(s, \Delta s) = \frac{|\Delta\boldsymbol{b}(s, \Delta s)|}{\sqrt{\langle|\Delta\boldsymbol{b}(s, \Delta s)|^2\rangle}}.$$

This is essentially a (positive definite) normalized magnitude of the increment. Note that the term PVI has been used in the literature to define both $\mathcal{I}$ and its square. The spatial average in the denominator is taken over some segment of the trajectory but at least several correlation lengths of the turbulence. For the analysis presented here, the authors averaged over $535\lambda_\mathrm{CS}$.

In figure 11, contour lines of the magnetic field from the 2D simulation are depicted along with identified current sheets (blue). The path s is the diagonal set of green solid lines. Since the simulation is performed in a periodic box, when the green trajectory leaves the right edge of the box, it re-emerges at the corresponding point on the left side of the box. A technique for statistically associating regions of high magnetic stress and tangential discontinuities with reconnection current sheets is employed using the PVI metric. Not all magnetic discontinuities in an experiment or simulation are active reconnection sites, but in a simulation, much more information can be brought to bear to identify a discontinuity as an active current sheet.

The idea is to set a threshold on the normalized increment in order to select the highest gradient discontinuities. In the figure, a threshold value of $\mathcal{I} \geqslant 5$ is selected. In other words, we wish to examine those tangential discontinuities with a gradient greater than about 5 standard deviations above the mean fluctuation. In the example, there are 40

discontinuities with $\mathcal{I} \geqslant 5$ of which 23 are active reconnection sites (determined by other criteria). In addition, there are a total of 37 identified active reconnection sites on the trajectory s, meaning that not all reconnection sites have a large enough PVI to be selected by the threshold. In any case, this simple statistical method associates regions of magnetic stress and discontinuity with active reconnection current sheets with about 50% efficiency.

An important next step is to associate turbulent heating with coherent structures as identified above as departures from Gaussian statistics. In a series of papers, Osman *et al* [31, 39, 40] have begun to associate enhancements in heating-related solar wind diagnostics with coherent structures. Their findings support the hypothesis that dynamically generated current sheets in the solar wind are sites of enhanced heating. The idea is to use the PVI diagnostic discussed above to conditionally average solar wind data, specifically heating diagnostics such as electron heat flux, electron temperature and ion temperature measured by the ACE and Wind spacecraft.

Osman *et al* made several interesting findings. First, conditional sampling on the PVI statistic shows enhancement in every heating-related diagnostic [31]. In particular, ion temperature measured by the ACE spacecraft showed an increase from 68, 000 K to 138, 600 K to 193, 200 K conditionally sampled on the PVI statistic for $\Delta B \leqslant 0.2\,\sigma$, $\sim 2\,\sigma$ and $\geqslant 3\,\sigma$ respectively. This is significant evidence that enhanced ion heating occurs in coherent structures with the highest heating occurring in the structures with the largest intervals ΔB. These structures are revealed as large discontinuities in the magnetic field that appear much more often than one would expect from a normal distribution of fluctuations.

Second, Osman *et al* found a preponderance of hot ions with a different association connected with the PVI interval statistic [39]. In a remarkable discovery, Bale *et al* [41] found that the distribution of 1 million gyroscale solar wind magnetic fluctuations from the Wind spacecraft when plotted in $T_\perp/T_\parallel$ versus $\beta_\parallel$ space are highly constrained by the mirror instability threshold at high $T_\perp/T_\parallel$ and the oblique firehose instability at low $T_\perp/T_\parallel$. There are essentially no observations of solar wind fluctuations at very large or very small $T_\perp/T_\parallel$ if $\beta_\parallel \geqslant 1$. Osman *et al* [39] analyzing the same data, found that near instability thresholds both the PVI statistic was large and the scalar proton temperature was enhanced by a factor of 3–4. There is a clear association of hot ions, enhanced PVI, and anisotropy instability thresholds in the solar wind.

Finally, Osman *et al* used measurements from the ACE spacecraft to provide evidence for non-uniform heating in the solar wind [40]. They measured the mean proton temperature conditioned on distance from high-stress magnetic events determined with the PVI statistic. Again, they found that the highest proton temperatures were associated with the largest increments. Furthermore, by estimating the thermal energy density of the solar wind conditioned on the PVI statistic, they found that a large fraction of the solar wind internal energy is due to heating in coherent structures constituting a relatively small volume of the plasma. For example, a PVI statistic of $\mathcal{I} \geqslant 2.4$ constitutes only 19% of the data set, yet is responsible for 50% of the heating.

2.2.4. Spatial structure function. For the same reason that spatial increments are challenging in observations and experiments, so are spatial structure functions. Indeed, accurate computation of structure functions, especially at high order, require very large data sets [42]. Experimental determination of high-order single time spatial structure functions, particularly in the solar wind, are challenging. Yet it is important that we study them since intermittency and the preponderance of small-scale coherent structures in a turbulent flow are revealed by the anomalous behavior of exponents of high-order spatial structure functions. In addition, predictions from turbulence theory typically refer to fluctuations in space. Spatial structure functions for the fluctuating magnetic field are defined in the same way as was done for temporal structure functions:

$$S_B^p(s, \Delta s) = \langle (\boldsymbol{b}(s + \Delta s) - \boldsymbol{b}(s))^p \rangle,$$

where s is a path through a turbulent flow. Hydrodynamic turbulence theory predicts that if the turbulence is self-similar and fully developed, then higher order structure functions should scale linearly with the order of the structure function: $S_B^p(\Delta s) \sim \Delta s^\zeta$. The Kolmogorov 1941 (K41) prediction for fluid turbulence is $\zeta = p/3$ [2, 3] while the Iroshnikov–Kraichnan (IK) prediction for MHD is $\zeta = p/4$ [43, 44]. The extent to which there is intermittency and coherent structures in the flow is manifest in departures from a linear relationship of the scaling exponents. Dissipation is likely to occur in these localized coherent structures whether they be viscous vortex filaments or resistive current sheets. Indeed, the dissipation need not be collisional but in the case of magnetic dissipation, almost certainly involves collisionless dissipation mechanisms at electron scales.

Again, we turn to MHD simulation for a suitable example [45, 46]. Mininni and Pouquet performed a turbulent, incompressible MHD simulation at high spatial resolution (1536^3). The simulation is run for 3.7 Alfvén times at the peak of dissipation then is stopped for analysis. At this time, the kinetic Reynolds number based on the integral (largest) scale of the flow is $R_e = 9200$ while the Reynolds number based on the smaller Taylor microscale is $R_e^{\text{eff}} = 1700$.

In figure 12, the scaling exponent ζ is plotted as a function of structure function order p. The scaling exponent for both magnetic and velocity fluctuations is plotted, as well as the K41 and IK predictions. A sample third-order structure function and fit is plotted above. The K41 prediction for third order is $\zeta = 1$. Note again that for $p = 2$ the K41 prediction is $\zeta = 2/3$ so that $S_B^2 \sim \Delta s^{2/3}$ and this implies a wavenumber power spectrum (also a second-order quantity) that varies like $E_B(k) \sim k^{-5/3}$. The slightly different scaling properties of the velocity and magnetic field are attributed to different intermittency properties of each field. Physically, a coherent magnetic structure leading to intermittency in the magnetic field would be a current sheet, perhaps at the boundary between magnetic flux tubes. A coherent velocity structure leading to intermittency in the velocity field would be a vortex structure, perhaps embedded in a sheared flow. The different geometrical character of these structures could explain the

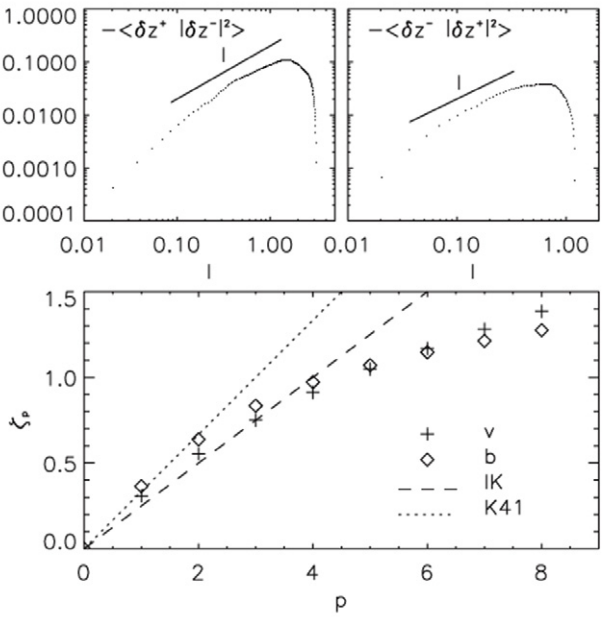

Figure 12. Spatial structure function. Slope of the spatial structure function for orders 1 to 8 from a 3D MHD simulation for both velocity and magnetic field (lower). Theoretical prediction from both Iroshinov–Kraichnan (IK) and Kolmogorov (K41) are plotted. The upper plot depicts the third-order structure function [46]. Reprinted with permission.

differences in the scaling properties and the spectra. Note that measurements in the solar wind show that velocity power spectra are slightly flatter than magnetic field power spectra for the same interval [47].

As an aside, there is now evidence that the magnetic spectrum in the solar wind with a power law exponent of 5/3 is somewhat steeper than the velocity spectrum with a power law exponent closer to 3/2 [47]. This would imply a second-order structure function $p = 2$ scaling exponent of $\zeta = 2/3$ for magnetic fluctuations but a scaling exponent of $\zeta = 1/2$ for velocity fluctuations. These results are due to careful analysis of four distinct intervals Wind spacecraft data with long records (up to 2.3 million samples). Power spectra for each of the three Cartesian vector components are summed to obtain a total power spectrum for velocity and magnetic fluctuations. This result points out that there are likely different transfer and dissipation mechanisms for kinetic and magnetic energy in a turbulent plasma. In particular, velocity fluctuations are damped by plasma viscosity parametrized by the kinetic Reynolds number R_e, while magnetic fluctuations can be damped by plasma resistivity parameterized by the magnetic Reynolds number R_m. The ratio, the Prandtl number $P_m \equiv R_m/R_e$, can take on any value.

3. Survey of turbulence experiments

There have been several excellent laboratory measurements of plasma turbulence in non-fusion devices. However, these have tended to focus on electrostatic drift wave turbulence in linear, magnetized plasma columns [48–51]. Because of the important role turbulence plays in transport, there have also been numerous studies of plasma turbulence in toroidal magnetic confinement fusion devices, including both electrostatic and magnetic fluctuations. For this survey, we have selected early studies in a tokamak [9] and in a reversed field pinch [18], and conclude with a more modern study of wavenumber magnetic spectra in the MST reversed field pinch [19, 20]. Our focus is on the use of the statistical turbulence tools discussed above (spectra, correlation functions, etc) rather than on the transport. Our emphasis will be on magnetic and velocity fluctuations, though we will discuss one measurement of electrostatic turbulence.

The energy injection process at the largest scales is different for every turbulent plasma. The notion of Kolmogorov-type turbulence is that once energy is injected into the inertial range, the memory of the injection process is lost and all that matters is the local transfer of energy from one scale to the next. However, in a plasma there are fluid processes that can rapidly couple energy from the very largest scales to the very smallest. For example, in an interesting MHD experiment it was shown by Moser and Bellan that a large-scale kink instability could drive a small-scale Rayleigh–Taylor instability [52].

Large-scale MHD processes can also destabilize small-scale kinetic processes. For example, in regions of high current density (say reconnecting current sheets) with electrons drifting at velocity v_D with respect to ions, electrostatic ion cyclotron waves with $\omega \cong \Omega_{ci}$ are destabilized if $v_D \gg v_i$ where v_i is the ion thermal speed [53]. These waves propagate across the magnetic field with $k_\perp \rho_i \cong 1$, where $k_\perp$ is the wave number orthogonal to the magnetic field and ρ_i is the ion's thermal gyroradius. The theory is appropriate for $\beta \ll 1$ and $T_e \cong T_i$.

Large-scale driving can be reconnection-type tearing modes (such as in the MST reversed field pinch) or supersonic acceleration of the solar wind at the corona. The driver for edge turbulence in a tokamak is typically gradients in density or temperature. Very specific types of electrostatic turbulence can be driven by ion-temperature gradients (ITG) or electron-temperature gradients (ETG) [54]. In the SSX MHD wind tunnel, the injection mechanism is the unraveling of magnetic energy stored in a compact, twisted structure called a spheromak.

3.1. An early tokamak study

We begin with a series of studies by Zweben *et al* in the mid-1980s of turbulence in a small research tokamak [9, 55]. Subsequent related experiments on several other tokamaks were covered in a review article by the same author [11]. The work presented here is prototypical of drift wave turbulence in many other devices. While the character of the turbulence in these experiments was electrostatic, the methods and analysis foreshadowed a more modern approach.

The Caltech tokamak was a small device with toroidal field $B_0 = 0.35$ T and plasma current $I = 30$ kA. The dimensions of the device were $R = 0.45$ m and $a = 0.16$ m. The density and temperature near the edge of the device (where measurements were made) were $n_e \cong 10^{12}\,\mathrm{cm}^{-3}$ and $T_e \leqslant 25$ eV. Two

Langmuir probe arrays were used. One linear array featured 32 tips each 1 mm in diameter. The other 2D array was an 8×8 matrix of probes covering a 1.8 cm square patch near the wall. Data were recorded with an analog bandwidth of about 200 kHz. Ion saturation current was recorded on each probe tip, proportional to the local electron density.

The key results were that the turbulence consisted of density and electrostatic potential structures aligned with the background toroidal field; essentially 2D filaments. Correlation lengths in the poloidal (r–θ) plane are short (about 1 cm) and fluctuation amplitudes are large ($\delta n/n \geqslant 5\%$). These types of structures are now known to be ubiquitous in toroidal confinement devices and have subsequently been measured and imaged in virtually every device [11]. In that recent review, Zweben states 'the size scale is typically ~0.1–10 cm perpendicular to the magnetic field but many meters along the magnetic field, i.e. the structure is nearly that of 2D filaments.' [11]

Using the same analysis tools described in section 2, Zweben *et al* find a de-correlation time from the autocorrelation function of about 100 μs and a correlation length from the spatial correlation function of about 1.2 cm (poloidal direction). Note that these are times and lengths associated with density fluctuations in the turbulence but the analysis techniques are identical to those used in section 2. The temporal and spatial correlation functions for this experiment are shown in figures 3(a) and (b) in [9]. Since they measured fluctuations with good spatial and temporal resolution, the authors were able to construct spectra using FFTs in both the time and space domains ($\tilde{n}(\omega, k)$, see figure 5 in [9]). No spectral indices are calculated.

Particularly interesting, and a harbinger of experiments decades later, 2D fluctuation maps were constructed to generate frame-by-frame 'movies' of the turbulence. At each time step a 2D map of the density fluctuations were constructed from the 8×8 array. Correlation functions in the radial and poloidal directions can be compared and they find that the radial correlation length is shorter (about 0.7 cm).

Electrostatic edge turbulence is observed in virtually every toroidal magnetic confinement device [11], and that turbulence has been implicated in degraded confinement of particles and energy. Turbulence has been mitigated in virtually every toroidal magnetic confinement device since 1982 by the application of sheared poloidal flow and so-called H-mode ('H' for high confinement) [16, 17]. The idea is that sheared poloidal flow at the edge (either driven by an applied radial electric field or spontaneously generated by other means) breaks up the larger eddies, de-correlates the turbulence, and mitigates radial transport. A transport barrier is generated at the edge, reducing diffusion to neoclassical levels.

More sophisticated statistical measures can be extracted from 2D fluctuation maps such as the third-order quantity: the auto-bispectrum [56]. The bicoherence (a normalization of the auto-bispectrum) is sensitive to the phase relationship among three waves ($\boldsymbol{k}_1 + \boldsymbol{k}_2 = \boldsymbol{k}_3$). If the phases of the three waves are not coupled, then the bicoherence is approximately zero.

3.2. An early reversed field pinch study

The first systematic measurements of magnetic fluctuations in a laboratory plasma were studied in the Zeta reversed field pinch at Culham by Robinson and Rusbridge in the early 1970s [18]. The study included variations in discharge current and toroidal field, but the biggest variations were observed with changing neutral fill pressure.

The authors propose in this paper that MHD turbulence bears a resemblance to conventional fluid turbulence, but with the turbulent elements elongated along the magnetic field (5 cm in radius but more than 60 cm long, aligned with the magnetic field). This suggests the paradigm of 2D turbulence as a model, very similar to that found for electrostatic turbulence in tokamaks [11], but now the structure is in the velocity and magnetic fields. It was the intention of the authors to examine the turbulence in Zeta in light of the Kolmogorov energy cascade picture. They say, 'nonlinear effects couple (large scale structures) to eddies of smaller scale and the turbulent energy cascades through ever smaller scales until on the smallest scales viscous damping becomes important and dissipates the energy into heat'. The seminal work of Robinson and Rusbridge is often cited in studies of anisotropic turbulence in the solar wind.

The Zeta reversed field pinch was a large fusion device operated at the Culham Laboratory in the United Kingdom for the UK Atomic Energy Authority. It had a toroidal field $B_0 = 0.15$ T and plasma current $I = 150$ kA. The dimensions of the device were $R \cong 1.8$ m and $a \cong 0.5$ m. The density and temperature near the center of the device were $n_e \leqslant 10^{14}$ cm^{-3} and $T_e \leqslant 15$ eV. Measurements of ion temperature were inconclusive, but it was suggested that T_i was substantially higher than T_e (as high as 400 eV from some early ion Doppler broadening measurements [57]). The densities and temperatures were similar to those measured in the SSX MHD wind tunnel discussed below, though in a device a factor of 5 larger.

Measurements were made with magnetic pickup loops about 0.5 cm in diameter consisting of 500 turns. The system (with integrators) had a bandwidth of about 1 MHz. The probes were placed in 1 cm diameter quartz tubes. Spatial resolution was about 1 cm. Dominant magnetic field fluctuations at 1–3 kHz were highly correlated at large scales and corresponded to helical distortions of the whole current channel. Higher frequency fluctuations above 7 kHz were correlated only over distances of $\leqslant$10 cm and could be analyzed as MHD turbulence.

While most of the turbulent energy was contained in fluid motions, measurements of velocity fluctuations with two-sided electrostatic probes proved difficult. It appears that there was some interference or ground loops affecting the electrostatic signal. Nonetheless, Robinson and Rusbridge conclude that the energy injection mechanism of the Kolmogorov cascade are large-scale velocity fluctuations such that $\boldsymbol{E}+\boldsymbol{v}\times\boldsymbol{B} \approx 0$. They note that since the electric field fluctuations are approximately curl-free (irrotational), then the velocity field fluctuations are approximately divergence-free (solenoidal).

Robinson and Rusbridge adopt the notation $\langle b_\alpha b_\beta \rangle_\gamma$ to denote the correlation between the α and β components of the

magnetic field separated in the γ direction. Figures 2 and 3 of [18] show the spatial correlation function $\langle b_r b_r \rangle_r$ for a variety of gas fill pressures and discharge currents. Using analysis similar to that discussed above, the authors fit the radial correlation function to a quadratic form in order to extract a Taylor microscale. Another technique uses the first-order structure function (normalized) to estimate the microscale. The microscale varies from a few cm to 6 cm in Zeta, with some dependence on fill pressure (figure 5 of [18]). Spatial correlation lengths in the radial direction are of the same order (about 5 cm) while correlation lengths along the field lines are much longer. The authors state, 'the turbulent elements must be thought of as rolls with length at least ten times the radius, aligned along the magnetic field'.

The frequency power spectrum for the magnetic field was measured in Zeta and fit to a power law. Note that since there is no bulk flow reported in Zeta ('the mean velocity of the plasma is negligible'), the connection between the frequency power spectrum and the spatial power spectrum is unclear (i.e. there is no Taylor hypothesis as discussed above). Nonetheless, the authors report steep power-law spectral indices between 3.4 and 6.4 for low (0.5 mTorr) and high (5.0 mTorr) fill pressure of deuterium (and decreasing Reynolds number). Autocorrelation functions were measured and autocorrelation times extracted for Zeta discharges. The authors find autocorrelation times for magnetic fluctuations on the order of 10 μs that increased with increasing fill pressure.

The authors calculate large-scale kinetic and magnetic Reynolds numbers, R_e and R_m, based on microscopic viscosity and resistivity and find a range from $R_e = 1000 \rightarrow 5$ and $R_m = 200 \rightarrow 1$ (see figure 12 of [18]). This variation follows an increase of fill pressure from $p = 0.1 \rightarrow 5$ mTorr. Note that this means that Zeta plasmas were somewhat more resistive than viscous (i.e. $Pr \approx 0.2$). If $T_\mathrm{i} \gg T_\mathrm{e}$, this result is difficult to explain. The authors then calculate the kinetic and magnetic microscales from R_e and R_m. These range from $0.03 \rightarrow 2$ cm and $0.1 \rightarrow 3$ cm (see figure 13 of [18]). These values are consistent with the calculated Reynolds numbers but inconsistent with the measured integral and microscales (which were found to be comparable). Recall that in section 2 we found that $R_\mathrm{Taylor} \sim (\lambda_\mathrm{int}/\lambda_\mathrm{micro})^2$.

The authors go to heroic lengths to estimate the normalized triple correlation $\langle v_1^2 v_2 \rangle$ and find a value of -0.016 ± 0.004 (statistically different than zero). This is the main result of the paper. They note that 'the triple velocity correlation in a flow is a measure of the nonlinear terms in the equation of motion and hence of the effectiveness of the transfer of energy between the different modes'. They claim that 'the existence of a triple velocity correlation combined with the form of the measured frequency spectra and derived wavenumber spectra invite comparison with the cascade theory of fluid turbulence'.

Ion Landau damping is suggested as a possible dissipation mechanism at low neutral fill pressures (and higher Reynolds number). Viscous damping is suggested as the dominant dissipation mechanism at higher pressures.

3.3. A modern measurement of the wavenumber power spectrum

The MST reversed field pinch is a large, modern magnetic confinement device with major radius 1.5 m and minor radius 0.5 m. The toroidal field is $B_0 \leqslant 0.5$ T and plasma current $I = 400$ kA. The plasma parameters of MST are much more fusion-relevant than the early Zeta RFP. The MST plasma density and temperature are $n_\mathrm{e} \sim 10^{13}$ cm^{-3} and $T \leqslant 2$ keV. With a strong toroidal field and low collisionality, MST achieves a Lundquist number up to 10^7. For the studies presented here, the plasma current was $I = 200$ kA and $T_\mathrm{e}(0) = 180$ eV [19, 20].

Turbulence in MST is driven by plasma relaxation and tearing mode activity at the largest scales of the device. Fully developed anisotropic magnetic turbulence ensues and is measured by magnetic probe arrays. The main finding is that the turbulence has broad spectral power in the direction perpendicular to the local mean magnetic field. The $k_\perp$ wavenumber spectrum is asymmetric in the ion and electron diamagnetic drift directions. The physical explanation is that a strong background magnetic field prevents bending of field lines, but it is easier to interchange or translate field lines as one would expect from waves propagating across the mean field.

The MST magnetic probe array has two sets of four coils (3 mm in diameter) which simultaneously measure the poloidal (r–θ) and toroidal components of the magnetic field. Note that in MST, the background field near the edge is largely in the poloidal direction. It is characteristic in a reversed field pinch for the toroidal field to reverse (hence the name), so that at the reversal layer, $B_\mathrm{tor} \sim 0$. Like the SSX MHD wind tunnel measurements discussed below, MST measures $\dot{B}$ directly to maximize bandwidth. Fluctuations up to 2.5 MHz can be measured.

Data are taken during a large relaxation event (sawtooth 'crash'). Local mean field is about 400 G ($f_\mathrm{ci} \sim 600$ kHz) while the fluctuation level during the 'crash' is about 50 G, so $\delta B/B \cong 0.1$. The MST data was presented in figure 10 in section 2. As noted above, the spectrum reaches into the dissipation range, so the authors perform a fit to a model that includes the characteristic Kolmogorov $k_\perp^{-5/3}$ scaling, as well as an exponential dissipation term:

$$E_B(k) = \epsilon^{2/3} k_\perp^{-5/3} \exp\left(-b(k_\perp/k_\mathrm{d})^\alpha\right).$$

Terry *et al* find a dissipation wavenumber $k_\mathrm{d} = 0.6\,\mathrm{cm}^{-1}$, suggesting dissipation at about the ion gyroscale of 1 cm in MST. Values of $\alpha = 4/3$ and $b = 3/2$ are consistent with theoretical models discussed in the paper [19]. In particular, the theory is extended to large magnetic Prandtl number $Pr = R_m/R_e = \nu/\eta$ (i.e. to plasmas that are more viscous than resistive, such as the SSX MHD wind tunnel plasma).

Another related experiment, though not in fully developed turbulence, was a measurement by Howes *et al* of the nonlinear interaction of two counter-propagating Alfvén waves [58]. This is the first demonstration of the 'building block' of Alfvénic turbulence: two waves coupling to produce a third at higher spatial and temporal frequency (i.e. smaller scales). The setup of the experiment is to launch two Alfvén waves at either end of the very long LAPD device (the plasma is 16.5 m

in length and 0.4 m in diameter). One wave is launched at high frequency (270 kHz) and the second at a much lower frequency (60 Hz). The polarization of the waves is orthogonal, and $k_{\perp 1}/k_{\perp 2} \sim 3$.

The amplitude of the parent waves is not large, but the observational signature of the non-linear daughter Alfvén wave is clear. The daughter wave has the predicted wavenumber from conservation of momentum: $\boldsymbol{k}_3 = \boldsymbol{k}_1 + \boldsymbol{k}_2$, at the expected frequency from conservation of energy: $\omega_3 = \omega_1 + \omega_2 \sim \omega_1$. The amplitude of the daughter wave was very small (10 mG cm^2) compared to the parent waves (500 mG cm^2 and 10 000 mG cm^2, respectively) so no further dynamics could be measured. Nonetheless, this is an important demonstration of the basic physics of Alfvén wave coupling.

4. MHD plasma wind tunnel

In this topical review, we have seen that a typical laboratory experiment exhibiting MHD turbulence features a large applied magnetic field generated by external coils. This is particularly true of devices designed for magnetic confinement fusion (e.g. reversed field pinch or tokamak), since a strong toroidal field is important for stability but does not participate in the dynamics. In naturally turbulent plasmas, such as the solar wind or a pulsar magnetosphere, the magnetic field is completely dynamical, meaning that the magnetic field is convected along with the plasma flow and is generated entirely from currents flowing in the plasma. In addition, natural plasmas have a wide range of plasma beta, $\beta \equiv (2\mu_0 nkT)/B^2$. The solar corona has $\beta \ll 1$, while the solar wind has $\beta \sim 1$. Natural plasmas tend towards equipartition of thermal energy, magnetic field energy, and flow energy.

In what follows, we present a description of the SSX MHD plasma wind tunnel. The salient features are first, that the MHD wind tunnel configuration has no applied magnetic field and has no net axial magnetic flux. Second, the plasma flow speed is on the order of the local sound speed ($M = 1$), so flow energy is comparable to thermal energy. Third, the plasma β (ratio of thermal to magnetic pressure) is of order unity so thermal energy is comparable to magnetic energy. The first section describes the operation of the plasma source, the second section describes diagnostic capabilities, and the third section provides some initial turbulence results from the SSX MHD plasma wind tunnel. Table 1 lists some of the main plasma parameters of the SSX MHD wind tunnel.

4.1. Operation

The Swarthmore Spheromak Experiment (SSX) [59] is a flexible facility used to study plasma merging and magnetic reconnection with a variety of boundary shapes. The SSX device features a $L \cong 1$ m long, high vacuum chamber in which we generate $n \geqslant 10^{20}$ m^{-3}, $T \geqslant 20$ eV, $B \cong 0.1$ T hydrogen plasmas. Plasma plumes are generated by pulsed magnetized plasma guns at either end of the device. Plasmas are accelerated to high velocity ($\cong 50$ km s^{-1}) by the discharge current in the guns ($\leqslant$100 kA) and injected into a highly evacuated target volume called a flux conserver. The flux conserver is usually cylindrical in shape and bounded by a thick, highly conducting copper shell. In a typical experiment, plasma plumes are injected at either end of a flux conserver and dynamical merging and relaxation ensue. From line-averaged measurements of n_e, T_e, T_i, and B, we measure a plasma beta in the wind tunnel of up to $\beta \sim 0.5$ [60].

Table 1. SSX MHD wind tunnel parameters.

Parameter	High energy	Low energy
B_0 (T)	0.5	0.1
n_e (cm^{-3})	10^{15}	10^{14}
T_e (eV)	10	20
T_i (eV)	20	40
β	0.03	0.2
ρ_i (cm)	0.1	0.6
c/ω_{pi} (cm)	0.7	2.3
V_{Alf} (km s^{-1})	350	220
f_{ci} (MHz)	7.6	1.5
R_m	150	425
S	2600	1670

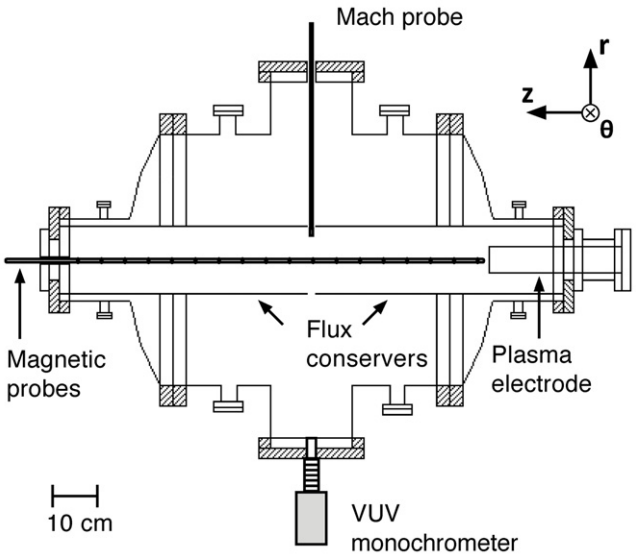

Figure 13. SSX plasma wind tunnel. Magnetized plasma plumes are launched by coaxial plasma guns into a flux conserving boundary. There is no applied axial magnetic field nor neutral fill gas.

For this study, we have implemented one plasma source in a high aspect ratio 'wind tunnel' configuration (see figure 13). The wind tunnel presently has dimensions $R = 0.08$ m and $L = 1.0$ m (about 20 l), but an extended length is planned. The plasma gun can inject a magnetized plasma plume of either right-handed (RH) or left-handed (LH) magnetic helicity from either end of the machine. Operationally, this means that the discharge current in the gun can be either aligned or anti-aligned with the magnetic field imbedded in the inner electrode (referred to as 'stuffing flux', Φ_{gun}, in prior work). The tungsten-coated inner electrode of the gun has dimension $r_{in} = 0.031$ m. The magnetic helicity of the plume also determines the helical pitch of magnetic field lines in the final relaxed state in the wind tunnel [61]. Colliding plasma plumes have also been studied but the dynamics are much more complex. Some initial results of colliding MHD plasmas are presented in the Results section below.

Plasma plumes are generated in the SSX wind tunnel by a discharge in a magnetized plasma gun. The operation is discussed in great length in the book by Bellan [62]. The gun is prepared with a fixed amount of magnetic flux emanating from its end. The guns and wind tunnel are highly evacuated initially. There is no fill gas, nor is there any applied axial magnetic field. Approximately 1 cc-atm of pure hydrogen (a few 10^{19} atoms) is puffed into the gun and high voltage is applied. Operationally, we delay firing the main discharge by 400–800 μs to allow less or more gas flow into the gun breach. We find that a delay of about 400 μs is optimal, allowing neutral gas to pressurize the gun region but not enough time for gas to propagate into the main wind tunnel chamber. Capacitor banks for the SSX plasma wind tunnel have $C = 1.0$ mF and can operate up to 10 kV (typically 4 kV at 8 kJ, high energy operation). The high voltage ionizes the gas and the subsequent high current (up to 100 kA) heats the plasma and ejects it out the gun. The stored energy in the plume is on the order of 1 kJ (0.5 T in a 20 l volume corresponds to 2 kJ).

Whether a plume of magnetized plasma emerges from the gun is a matter of pressure balance. Essentially, the magnetic pressure in the gun must exceed the magnetic tension in the stuffing flux. Very approximately, if we equate the magnetic energies, we find:

$$B_{\rm gun} = B_{\rm stuff} \rightarrow \frac{\mu_0 I_{\rm gun}}{2\pi r_{\rm gun}} = \frac{\Phi_{\rm gun}}{\pi r_{\rm gun}^2},$$
$$\lambda_{\rm gun} \equiv \frac{\mu_0 I_{\rm gun}}{\Phi_{\rm gun}} = \frac{2}{r_{\rm gun}}.$$

More sophisticated analysis yields a coefficient slightly different from 2, but the so-called stuffing threshold of the gun $\lambda_{\rm gun}$ is a constant of order unity (often a Bessel function zero) divided by a gun dimension (typically the radius of the inner or outer electrode). Geddes *et al* calculated a threshold for an early incarnation of SSX plasma gun and obtained $\lambda_{\rm gun} = (1/r_{\rm in})\sqrt{2/\ln(r_{\rm out}/r_{\rm in})}$ [63]. This makes the threshold about $\lambda_{\rm gun} = 46\,{\rm m}^{-1}$.

We have measured the stuffing threshold for this configuration by scanning the stuffing flux and gun current, then making a measurement of magnetic field downstream. Our metric for an unstuffed gun is the average magnetic field at the midplane of wind tunnel after a fully relaxed configuration was formed. For this experiment, we used $C = 0.5$ mF (low energy operation). In figure 14, we plot the mean midplane magnetic field as a function of gun current (actually $\mu_0 I_{\rm gun}$) and stuffing flux. It is clear that for large stuffing flux, no field is measured downstream. This is the 'stuffed' condition. There is also a clear threshold above which magnetized plasma emerges from the gun. The measured stuffing threshold is close to $50\,{\rm m}^{-1}$. Note that the model above predicted $\lambda_{\rm gun} = 46\,{\rm m}^{-1}$ [63] while $3.83/r_{\rm gun} = 48\,{\rm m}^{-1}$ [62], where 3.83 is the first zero of the Bessel function J_1, both very close to the measured value.

Note that moving to different operation points around the $\mu_0 I_{\rm gun}$ versus $\Phi_{\rm gun}$ plane is effectively a scan of the helicity content of the injected plasma. This is because the value of λ in the relaxed configuration is the eigenvalue of the force-free condition $\nabla \times B = \lambda B$. It is also the ratio of the magnetic

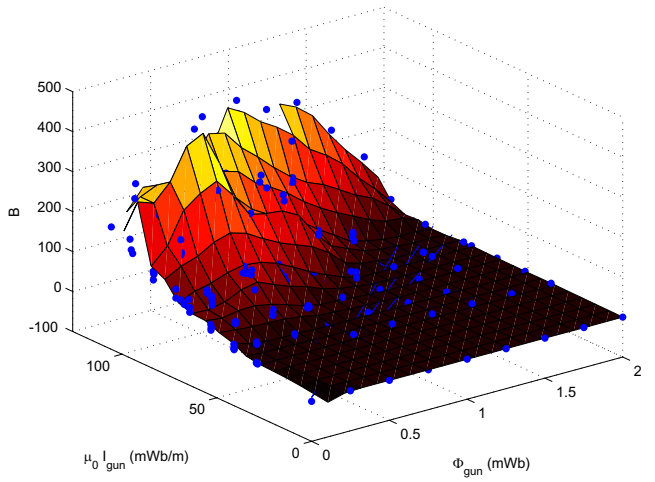

Figure 14. Stuffing threshold. Mean magnetic field at the midplane of the SSX wind tunnel for a relaxed plume, as a function of gun current and stuffing flux. Note that for very high stuffing flux, no field is measured downstream (stuffed condition). The measured stuffing threshold (the diagonal boundary between stuffed and unstuffed) is close to $50\,{\rm m}^{-1}$.

energy to magnetic helicity of the configuration: $\lambda \sim K/W_B$. We have found that the helicity content of the plasma plume has the biggest effect on turbulent intermittency [64].

A cryogenic pump provides the high vacuum (10^{-8} Torr) for the plasma wind tunnel. The interior walls of wind tunnel are maintained by helium glow discharge conditioning (GDC) consisting of a dc discharge at 0.1 A, 400 V with about 50 μm of He and baking with a thermal blanket (100 °C) for several hours. In order to clean the Langmuir and Mach probes, probe tips are biased during He glow to collect ion current. We find that the plasma wind tunnel and probe need to be glowed and baked again after 30–60 discharges for best results. All discharges in this study had similar external parameters: $I_{\rm gun} = 80$ kA, $\Phi_{\rm gun} = 1.0$ mWb, $W_{\rm bank} = 8.0$ kJ for the plasma source.

4.2. Diagnostics

General plasma diagnostics are discussed in textbooks [65], but diagnostics appropriate for plasma turbulence studies have particular demands. First and foremost, we require a diagnostic suite with high bandwidth. To be specific, the time cadence should be fast enough to resolve the physics of interest. The proton cyclotron frequency in a typical laboratory magnetic field of 0.1 T is 1.5 MHz. Each of the diagnostics below has bandwidth of at least 1 MHz so that physics beyond the proton gyrofrequency can be studied. Next, we would like the measurement to be local and non-perturbative. It is difficult to satisfy both requirements with the same diagnostic, so local probes (such as magnetic probes, Mach probes and Langmuir probes) should be as small as possible. Non-perturbative diagnostics (such as a density interferometer, or a spectrometer) tend to provide line-averaged information. Finally, and importantly for a laboratory turbulence experiment, it is useful if turbulent quantities could be probed at multiple locations in the plasma and at high

spatial resolution. This is a capability that is difficult in space plasmas (the tetrahedral Cluster satellite formation is the notable exception), but straightforward in a laboratory.

For each diagnostic used in the SSX plasma wind tunnel, we provide a brief description (with references), and a discussion of the turbulent quantities measured (also with references). Some example data is presented here, and more a detailed sample of turbulence measurements are presented in the following Results section.

4.2.1. Gun diagnostics. The source for the turbulent plasma plume is the coaxial magnetized plasma gun discussed above. The gun, cabling, ignitron switch and capacitor form a dynamic LRC circuit. Typically, the inductance of the circuit will change during the discharge as plasma runs along the gun. It is important to monitor gun parameters ($I_{\rm gun}$, $V_{\rm gun}$, $\Phi_{\rm gun}$) during each discharge so that quantities such as input energy ($\int I_{\rm gun} V_{\rm gun} {\rm d}t$), gun impedance ($V_{\rm gun}/I_{\rm gun}$) and input helicity ($\int \Phi_{\rm gun} V_{\rm gun} {\rm d}t$) can be computed later.

Gun current is monitored with a simple Rogowski coil on each bank [65], calibrated with a known low-inductance resistive load and a precision voltage probe. Generally, high bandwidth is not required for gun current measurements. Dynamic gun voltage requires a precision, compensated high voltage probe; a simple voltage divider typically has insufficient bandwidth. Since plasma, magnetic energy, and magnetic helicity can be injected in episodically from the source, $V_{\rm gun}$ can have a dynamic character with fluctuations in the MHz range. The gun flux that permeates the inner electrode operates on a much longer time scale (0.1 s) and so is essentially constant during the 100 μs discharge. $\Phi_{\rm gun}$ is measured with a simple flux loop. Results from measurements of $\mu_0 I$ and $\Phi_{\rm gun}$ were presented in figure 14. Based on measurements such as these, we have tended to operate the SSX wind tunnel around $I_{\rm gun} = 80$ kA, $\Phi_{\rm gun} = 1.0$ mWb, near the peak of the ridge in figure 14.

4.2.2. Magnetic probe array. Our principal measurement in the SSX MHD wind tunnel is that of magnetic fluctuations. Several aspects are critical for the design of a magnetic probe array. First, we require high spatial resolution and coverage spanning a correlation length. We also want to minimize the perturbation to the flow, so we opt for a single linear array of 16 probe triplets, separated by 4 mm. Second, we would like to maximize bandwidth so we use a single turn of magnet wire for each detector (3 mm inner diameter) to minimize self-inductance, and we encase the array in a quartz jacket to ensure rapid penetration of flux. We record $\dot{B}$ directly. Finally, we use 65 MHz, 14 bit DTAQ digitizers to ensure high bandwidth and sensitivity. A sensitivity of 14 bits corresponds to 2^{14} or about 16 000 levels, so we can measure fields from less than 1 G to over 1 T.

In the past, we have fielded as many as 600 individual magnetic probes in SSX experiments [66]. The full three-dimensional structure of reconnection events was mapped [67]. Those measurements tended to be of coarser resolution both spatially (about 2 cm) and temporally (about 1 μs). In addition, the jackets were thin-walled stainless steel, so that the magnetic flux penetration time was not instantaneous. For the studies presented here, we have opted for a single linear probe array with the smallest possible perturbation to the flow. Turbulence data from a magnetic probe is presented in the Results section.

Careful calibration of the magnetic probe array is important and is described in detail in prior papers [63, 66]. The essential idea is to construct a calibration matrix $\mathcal{C}$ that converts an array of measured voltages into a proper set of magnetic field components. The SSX MHD wind tunnel uses a carefully constructed Helmholtz coil set driven by the same pulsed power supply that energizes the plasma guns. We also use the same cabling and digitizer channels for calibration as we use for the experiment. It is important that the geometry of the Helmholtz coil is well known, as well as the current flowing in the coil. The probe array should be registered carefully with respect to the Helmholtz coil, so that coil locations are known in the Helmholtz coil coordinate system to within 1 mm. We use a Delrin jig designed to bolt directly to the Conflat vacuum fitting on the probe array. A high-resolution digital photograph of the Helmholtz coil and probe array with a ruler is very useful.

The Helmholtz coil should be constructed to minimize error fields from connectors and leads. It is important that there is no metal near the calibration jig to minimize image currents that perturb the Helmholtz field. Our Helmholtz coil support structure is constructed entirely of Delrin. Care must be taken to prevent ground loops that can pick up stray flux during calibration. For example, we isolate each connection at the probe housing to prevent forming a ground loop in the shields of adjacent probes. We estimate that our cumulative calibration error is about 1%.

The calibration technique consists of pulsing the Helmholtz coil with the magnetic probe array oriented successively in three orthogonal directions. A particular probe triplet in the array (with three orthogonal loops wound on precision Delrin forms) will sense signal in the three orthogonal directions. The computed field components $\dot{\boldsymbol{B}}$ and the corresponding offset subtracted signals V measured for these three shots with the Helmholtz pair determine all nine unknowns in the calibration matrix $\mathcal{C}$ for each probe triplet ($\dot{B} = \mathcal{C}V$). If the probes are wound carefully, and if the Helmholtz coil is well designed, then the calibration matrix is nearly diagonal. In practice, there is inevitably some misalignment of the triplet and some mixing of the signals. High frequency response of the probe/cabling system is checked with a separate, small coil and oscillator. We find flat response to about 4 MHz, and modest roll-off at higher frequencies. Since the system is linear, a careful calibration results in a very useful diagnostic.

4.2.3. Mach probe. Local velocity measurements are performed with a Mach probe. The essential idea is that ion current is collected on opposing faces of the probe. The component of the plasma velocity in the direction connecting the upstream and downstream faces is proportional to $\ln(J_{\rm up}/J_{\rm down})$. The proportionality constant is a matter of some controversy, but is of order unity. If high bandwidth current transformers are used, this diagnostic can be useful at very high frequencies (over 10 MHz). The Mach probe reports

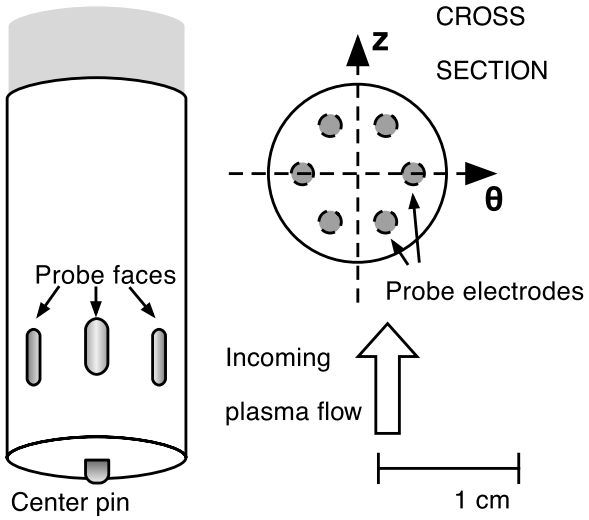

Figure 15. SSX Mach probe showing orientation of the electrode collector areas and device coordinates.

Mach number strictly speaking, so a measurement of the true flow speed (and fluctuations) requires a measurement of the electron temperature.

The SSX Mach probe has a cylindrical Gundestrup geometry in which six evenly spaced tungsten electrodes are encased in a boron nitride turret (see figure 15) [68]. The ceramic turret is 2.54 cm in length and 1.3 cm in diameter. The electrode collector faces are recessed into the ceramic housing by 2.0 mm to facilitate directionality. Each rectangular opening has length 4.0 mm, width 1.6 mm and area $A = 6.0 \pm 0.1\,\mathrm{mm}^2$. Individual electrode collectors effectively provide independent current measurements when biased with respect to the central pin, which protrudes from the end of the turret 1.6 mm. The exposed electrode collector areas are the same within 2%.

Each collector is biased using a separate 180 μF capacitor bank charged with an external power supply that is isolated during the plasma discharge to prevent ground loops. The voltage droop is typically less than 1% during a discharge so the voltage at each collector face is fixed. Six matched, high bandwidth (20 MHz) current transformers (Pearson model 411), one for each collector face, report the ion current from each probe face. The SSX Mach probe has been calibrated using time-of-flight and other means [68]. We find $J_{\mathrm{up}}/J_{\mathrm{down}} = \mathrm{e}^{KM}$ with $K = 2.0 \pm 0.5$. Turbulence data from the Mach probe is presented in the Results section.

4.2.4. Double Langmuir probe. Local density measurements are performed with a double Langmuir probe [69]. Langmuir probes are simple to construct and report information from regions as small as 1 mm. A time series of ion saturation current is a good proxy for electron density. We have used a double Langmuir probe on the SSX MHD wind tunnel to measure radial profiles of electron density and temperature, as well as local density fluctuations.

A useful aspect of a double Langmuir probe with identical electrodes is that the I–V characteristic is symmetric. Since the entire circuit floats with the plasma, and if there is no potential difference between the electrodes, there cannot be any current drawn so $I(0) = 0$ (if the plasma is quiescent). Furthermore, since the current has the same magnitude (opposite sign) at $\pm V$, the maximum current is limited by the ion flux. The I–V characteristic has the form [69]

$$I(V) = I_{\mathrm{sat}} \tanh\left(\frac{eV}{2kT_{\mathrm{e}}}\right),$$

where the maximum current is given by

$$I_{\mathrm{sat}} = neA\langle v\rangle = neA\sqrt{\frac{kT_{\mathrm{e}}}{M_{\mathrm{i}}}}.$$

Note that for voltages much less than an electron temperature ($eV \ll kT_{\mathrm{e}}$), $I(V)$ is approximately linear:

$$I(V) \cong I_{\mathrm{sat}}\left(\frac{eV}{2kT_{\mathrm{e}}}\right) = \frac{ne^2A}{2\sqrt{kT_{\mathrm{e}}M_{\mathrm{i}}}}V.$$

The full form may be written as

$$I(V) = neA\sqrt{\frac{kT_{\mathrm{e}}}{M_{\mathrm{i}}}}\tanh\left(\frac{eV}{2kT_{\mathrm{e}}}\right).$$

The SSX double Langmuir probe consists of two 1 mm diameter, 1 mm tall exposed tungsten tips emerging from an alumina ceramic shaft. Tip separation is about 1 mm. Probe tips were oriented across the flow direction to prevent one tip from shadowing the other. Probe position was incremented in 1 cm steps beginning at the edge of the cylindrical wall ($R = 78$ mm) for a total of six positions. We found that averaging five shots at each setting gave satisfactory statistics.

The probe tips are biased using an isolated 500 μF capacitor bank charged with an external power supply that is isolated during the plasma discharge to prevent ground loops. The voltage droop is typically less than 1% after a discharge so the voltage between the probe tips is nearly constant. The dynamical voltage difference between tips is monitored with a Tektronics isolated voltage probe during a shot. A high bandwidth (20 MHz) current transformer (Pearson model 411) reports the ion current flowing between the probe tips. Typical ion current magnitudes were 1–4 A consistent with $I = nev_{\mathrm{th}}A$.

The voltage between probe tips was scanned at −20, −10, 0, 5, 10, 15 and 20 V with five pulses of the wind tunnel at each voltage setting. Temperature and density are extracted from fits to the tanh function above. Six radial positions were scanned from $R = 78$ mm to $R = 28$ mm in 10 mm increments (a total of over 200 discharges). We present radial profiles of temperature and density relatively early in the discharge. We are interested in the spatial profile of the leading edge of the plume for studies of interactions with obstacles and plume–plume merging studies. In figure 16, we show the radial profile of temperature at $t = 33\,\mu$s, $T_{\mathrm{e}}(r)$. We note that the temperature profile is peaked on axis, with a hot core of $T_{\mathrm{e}} = 35$ eV on axis. A possibility is that hot plasma from the center electrode of the plasma gun persists to the midplane but we have strong evidence that the plume is not axisymmetric when it reaches the midplane [61]. The magnetic structure is close to a twisted Taylor double helix.

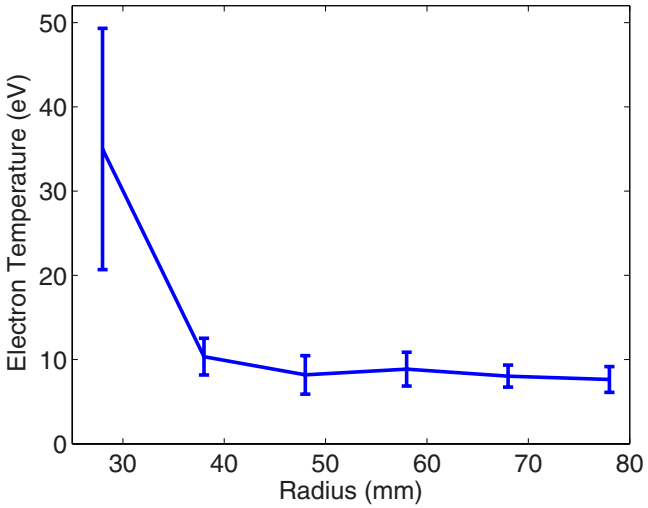

Figure 16. Measurement of the radial temperature profile of the SSX MHD wind tunnel plasma plume early in the discharge $t = 33\,\mu$s.

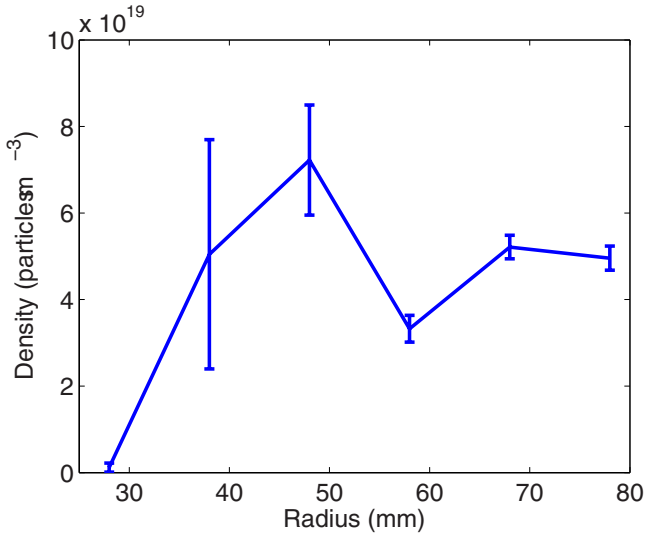

Figure 17. Measurement of the radial density profile of the SSX MHD wind tunnel plasma plume early in the discharge $t = 33\,\mu$s.

In figure 17, we show the radial profile of density at $t = 33\,\mu$s, $n_e(r)$. We note that the density profile is hollow on axis, with nearly an order of magnitude drop near the center of the flux conserver. Again, it is likely that we are sampling the plasma in a magnetic lobe of our twisted helical geometry.

4.2.5. HeNe interferometer. It is useful to have a non-invasive diagnostic for turbulence studies. Unfortunately, as noted above, non-invasive diagnostics are generally non-local. The SSX plasma wind tunnel employs a He–Ne laser quadrature interferometer for measurements of line-averaged density [70]. The technique uses a modified Mach–Zehnder configuration with a linearly polarized scene beam and a circularly polarized reference beam. The beams are de-coupled at the output using a Wollaston prism which generates signals proportional to the sine and cosine of the phase shift introduced by the plasma. The use of a circular polarizer in the reference beam effectively creates two coaxial linearly polarized beams (shifted in phase by $\pi/2$) so that the absolute phase shift due to the passage of the plasma plume can be unambiguously measured. The Wollaston prism separates the mixed circularly polarized beam into its two linearly polarized constituents (sine and cosine). The absolute phase is simply the arctan of the ratio of the signals. In a typical experiment at SSX, the scene beam passes through the plasma wind tunnel across a diameter (0.16 m), sampling plasma in a few mm wide beam. Turbulence data from the interferometer is presented in the Results section.

4.2.6. Soft x-ray array. A relatively simple non-invasive diagnostic but with a non-trivial interpretation is a soft x-ray (SXR) detector [71]. The SXR array on the SSX plasma wind tunnel consists of a matched set of four International Radiation Detectors AXUV silicon p–n junction (PIN) photodiodes filtered by thin films of aluminum 100 nm thick, titanium 50 nm thick, tin 100 nm thick, and zirconium 100 nm thick. The variation in the spectral response functions of the filters at EUV and SXR energies allows us to garner information not just about the time-dependent intensity of the SXR emission, but also about broad spectral properties of the emission. The SXR is sensitive to significantly higher energy photons than a VUV monochromator, and thus can potentially measure emission from hotter plasma and even emission produced by a possible high-energy, non-Maxwellian component of the electron population.

The signal measured on the SXR array comes from a complex physical process that is difficult to unravel, particularly with only a few channels. Emission in a particular energy band depends on the square of the electron density (and/or the product of electron density with impurity density), as well as some function of the electron temperature ($T_e^{1/2}$ for bremsstrahlung). In addition to thermal bremsstrahlung, emission can come from line radiation of partially stripped ions [71]. The use of the SXR is generally limited to total SXR light intensity as a proxy for fast electron population. Turbulence data from the SXR array is presented in the Results section.

4.2.7. Ion Doppler spectrometer. In the SSX plasma wind tunnel, radial flows and ion dynamics are monitored by our ion Doppler spectroscopy system (IDS, figure 18) [72]. This is another example of a non-invasive diagnostic. Impurity ions are entrained in the flow and the line-integrated motions are measured with IDS. The SSX IDS instrument measures the width and Doppler shift of either the nascent C_{III} impurity 229.7 nm line or a doped He_{II} impurity 468.6 nm line to determine the temperature and line-averaged flow velocity. The velocity resolution of the instrument is $\leqslant 5\,\mathrm{km\,s^{-1}}$, and the instrument temperature is about 3 eV. There is enough signal to resolve the full line within an MHD dynamical time (about $1\,\mu$s in SSX) for every discharge. Peak ion temperatures of 80 eV have been recorded during reconnection events as well as bi-directional outflows up to $\pm 40\,\mathrm{km\,s^{-1}}$ [73]. During reconnection and merging, we measure a period of reconnection-driven ion heating with peak temperatures for carbon $T_C \cong 50$ eV and for helium $T_{He} \cong 70$ eV (averaged over many shots).

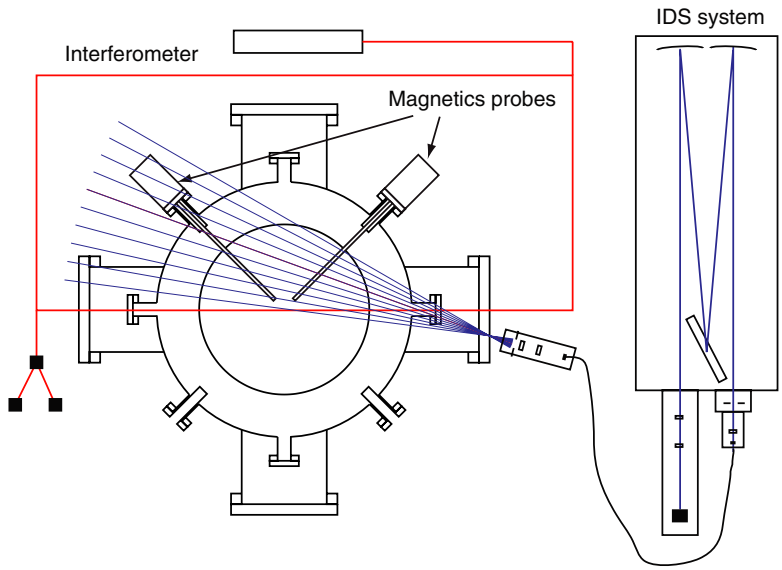

Figure 18. Ion Doppler spectroscopy in SSX. Cutaway end-view shows multiple chords for IDS, location of two typical magnetic probes (non-conducting quartz jacketed), and chord for HeNe interferomenter. Our prolate 0.6 m long, 0.4 m diameter flux conserver is depicted here.

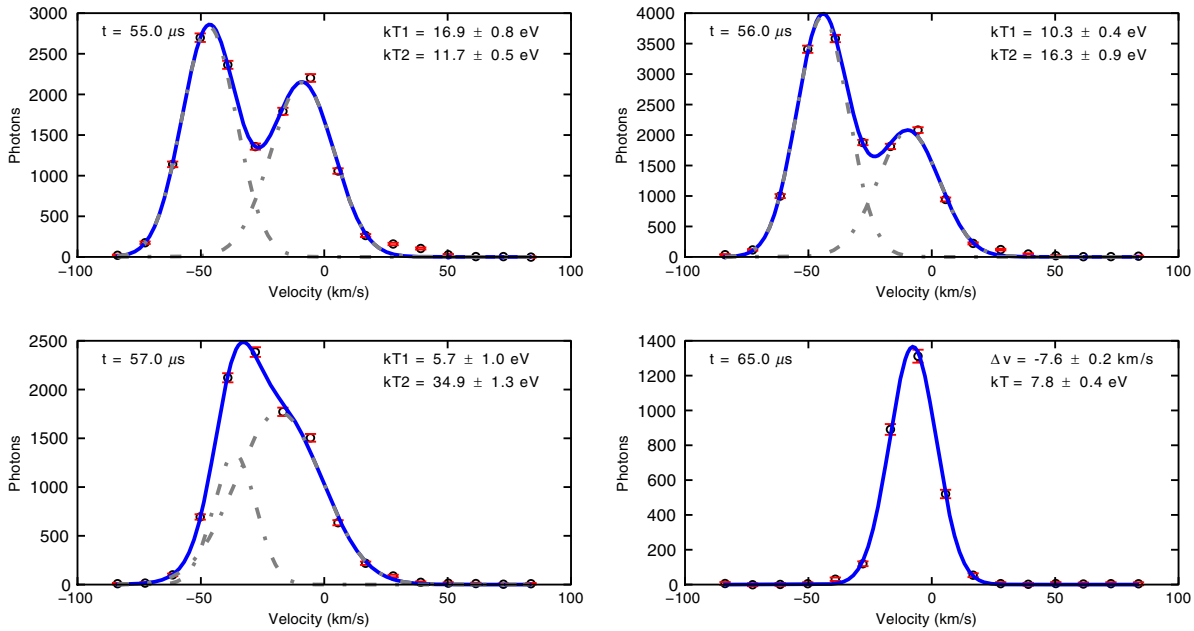

Figure 19. IDS data from a reconnection event in SSX. The first three panels show dynamical flows up to 50 km s^{-1} in 1 μs time increments during a reconnection event. The last panel shows a quiescent warm plasma in a relaxed state late in the discharge (8 eV).

The SSX IDS system employs two key features [72]. First, an echelle diffraction grating operating at 25th order provides high spectral resolution ($R \equiv \lambda/\delta\lambda = 2.5 \times 10^4$). Second, a multi anode photomultiplier tube array (32 channels) provides fast time response from the UV to the visible. The time resolution is about 1 μs limited primarily by photon statistics. The SSX IDS instrument is built around a McPherson Model 209 spectrometer. This is a 1.33 m focal length Czerny–Turner spectrometer with spherical collimating and focusing mirrors (Al–MgF_2 coated) and optimized for spectral resolution. The echelle grating is ruled at 316 mm^{-1} groove density with a blaze angle $\theta_b = 63.43°$. Calibration and alignment procedures are discussed elsewhere [72].

An example of IDS data is presented in figure 19. The first three panels show radial outflows up to 50 km s^{-1} during a reconnection event resolved in 1 μs increments. Later in the discharge, the SSX plasma has relaxed and cooled to about 8 eV. Turbulence data from the IDS is presented in the Results section.

4.3. Initial turbulence results

Here we present some initial turbulence results from the SSX MHD plasma wind tunnel featuring the diagnostics and techniques discussed above. Some prior work particularly on intermittency scaling with magnetic helicity has already

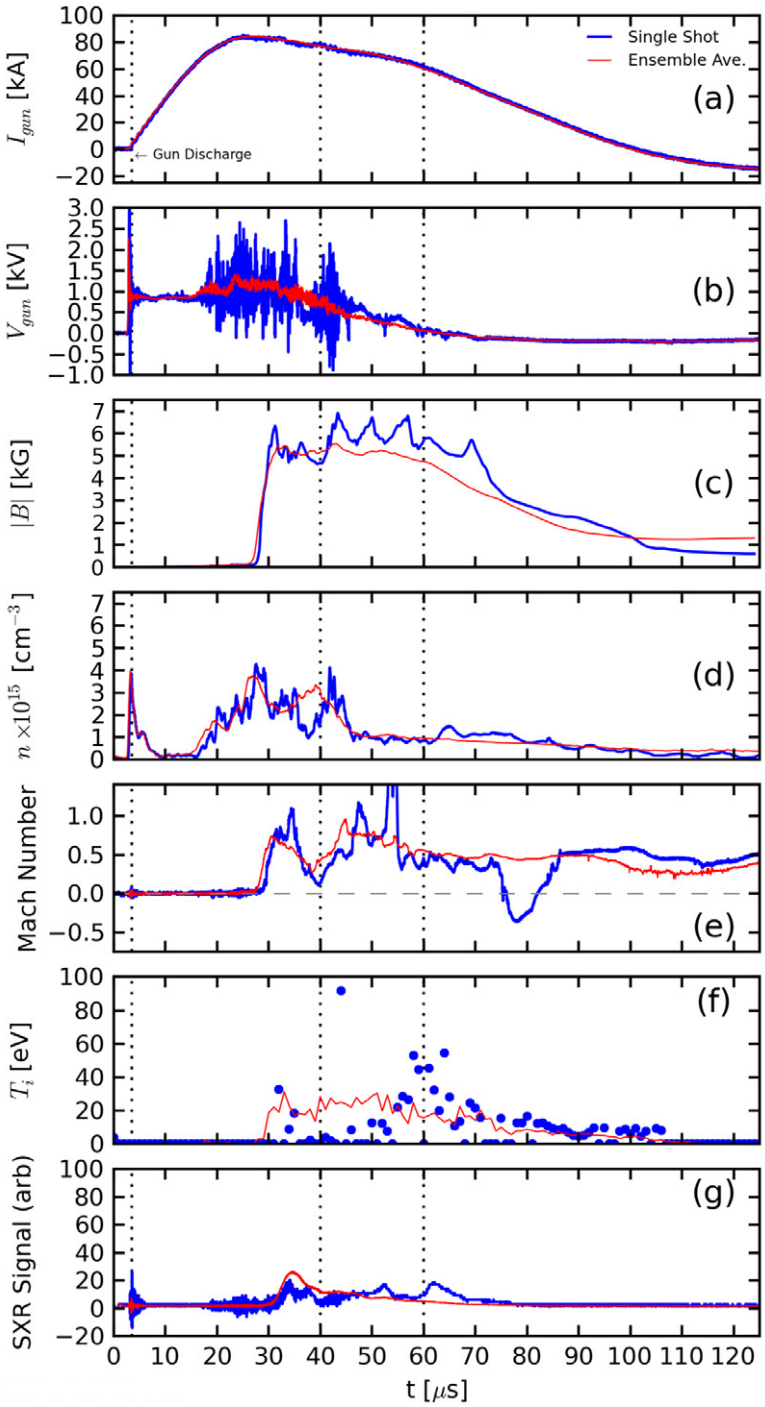

Figure 20. Time series for typical single plume: (*a*) discharge current, (*b*) discharge voltage, (*c*) magnetic field, (*d*) density, (*e*) Mach flow, (*f*) ion temperature and (*g*) SXR signal. Each panel shows an ensemble average of 40 shots (red) and a single shot (blue).

appeared [64, 74]. We focus on time series data here. Figures 20 and 21 show time series for seven diagnostics on SSX: discharge current, discharge voltage, magnetic field, density, Mach flow, ion temperature and SXR signal. The SXR signal is from the Al-filtered PIN diode (20–80 eV photons). Figure 20 shows an ensemble average of 40 shots (red) and a single shot (blue) for a typical 1.0 mWb stuffing flux, 4 kV, 8 kJ single plume discharge. Figure 21 shows the same time series plots but for zero stuffing flux. We note that gun current time series are similar in both cases, without much variability. In figure 20(*b*) there is a period of about 15 μs of a steady voltage of about 1 kV. This is an inductive voltage corresponding to the steady ejection of toroidal magnetic flux at a rate of about 1 mWb per μs. At $t = 20$–$30\,\mu$s there are large fluctuations in gun voltage corresponding to the detachment of a plasma plume. Note that the detachment occurs when $I_{\rm gun} = 80$ kA, so that the gun parameter is $\lambda_{\rm gun} = \mu_0 I_{\rm gun}/\Phi_{\rm gun} \cong 100\,{\rm m}^{-1}$, well above the stuffing

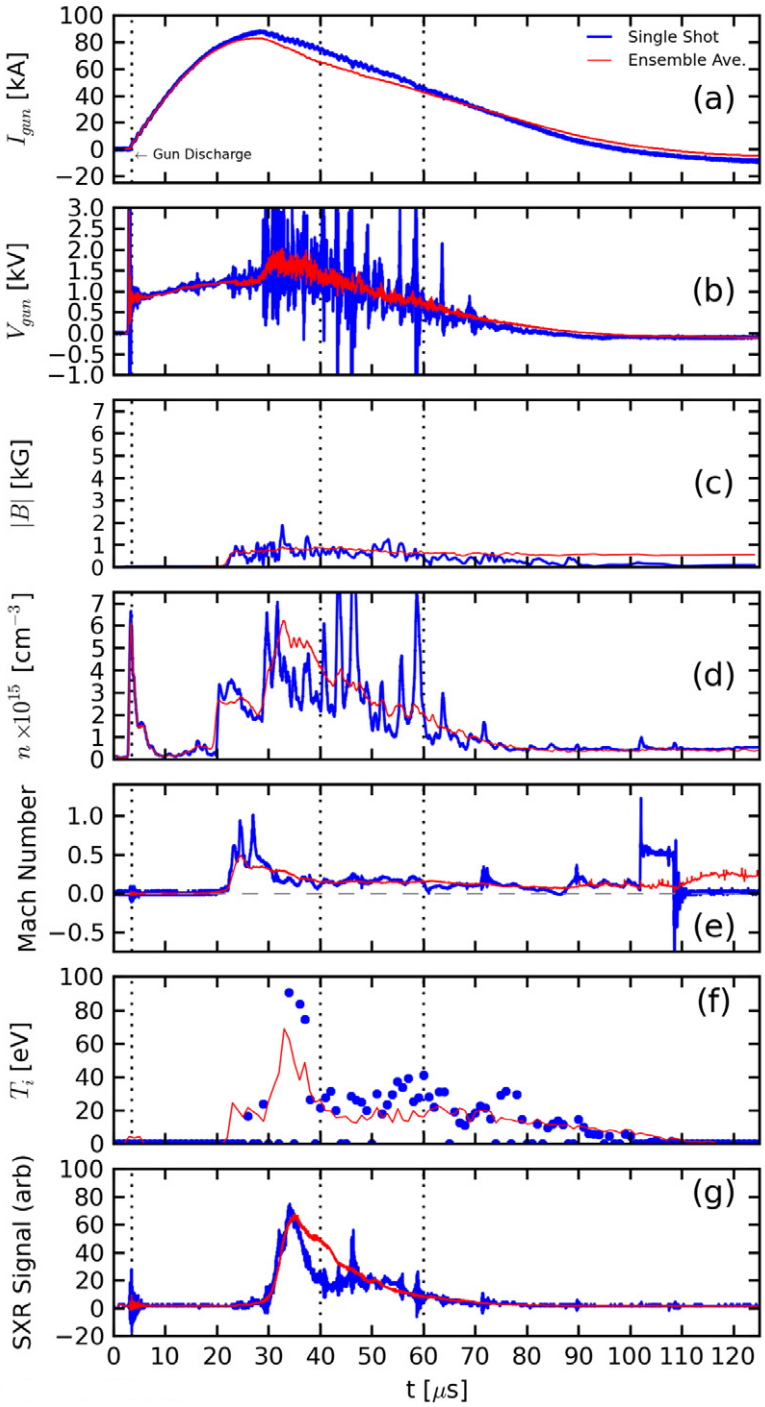

Figure 21. Time series for low flux single plume: (*a*) discharge current, (*b*) discharge voltage, (*c*) magnetic field, (*d*) density, (*e*) Mach flow, (*f*) ion temperature and (*g*) SXR signal. Each panel shows an ensemble average of 40 shots (red) and a single shot (blue).

threshold discussed above. The injected energy is on the order of $\int V_{\rm gun} I_{\rm gun}\,{\rm d}t \sim 1\,{\rm kV} \times 80\,{\rm kA} \times 30\,\mu{\rm s} \cong 2400\,{\rm J}$ (magnetic, flow and thermal). The injected helicity is on the order of $\int V_{\rm gun}\Phi_{\rm gun}\,{\rm d}t \sim 1\,{\rm kV} \times 1\,{\rm mWb} \times 30\,\mu{\rm s} \cong 30\,\mu{\rm Wb}^2$ [64]. Note that the ratio $\mu_0 W/K = \mu_0\, 2400\,{\rm J}/30\,\mu{\rm Wb}^2 = 100\,{\rm m}^{-1}$.

In panel (*c*) of both figures depicts magnitude of the magnetic field $|B|$ at one point near the axis of the wind tunnel at the midplane. The mean field from the ensemble average is about 0.5 T for the typical single plume condition, and nearly constant during the stationary phase of the turbulence (40–60 μs, indicated by the dotted vertical lines). The fluctuations are large, however, with $\delta B/B \sim 0.2$. The magnetic structure appears at the midplane about 10 μs after detachment from the gun about 0.5 m upstream, so the flow speed is roughly 50 km s^{-1}. The corresponding signal on the low flux, low helicity shot is much smaller, about 0.1 T.

In panel (*d*), we show the line-averaged electron density as a function of time. Plasma density appears before magnetic field because the interferometer chord is upstream of the

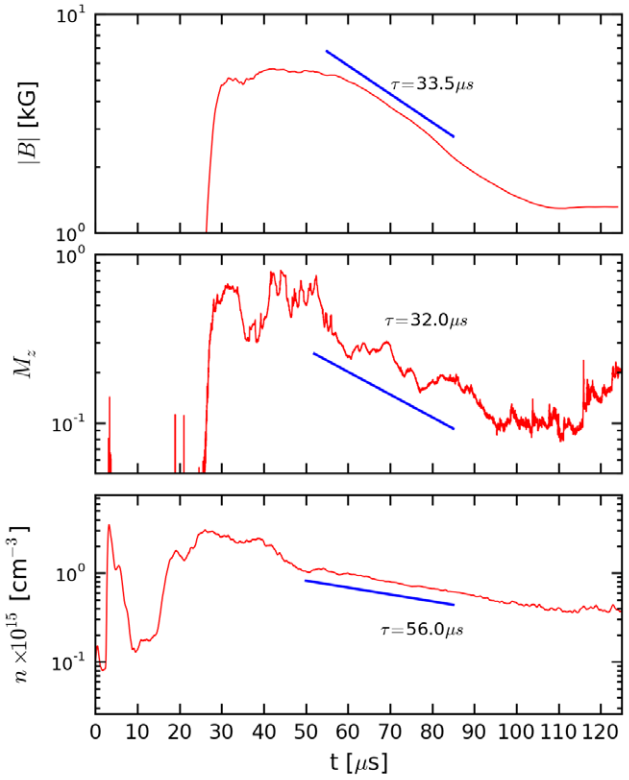

Figure 22. Average decay data. Top panel is $|B|$, middle is Mach flow M_z, lower is density.

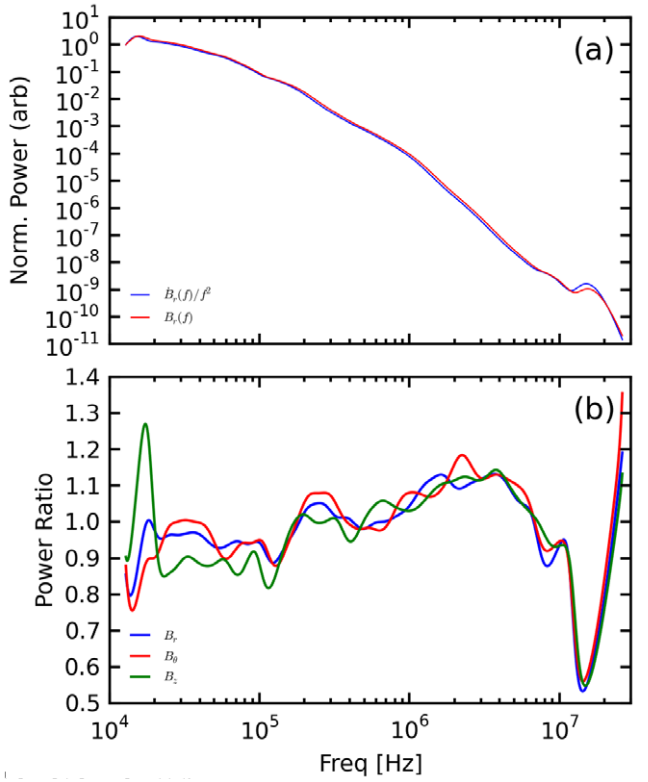

Figure 23. Comparison of spectra for raw $\dot{B}$ versus integrated B.

midplane. The HeNe beam is passed through a small hole in the flux conserver wall, so the distance over which the density is averaged is the diameter of the wind tunnel. The density for the low flux case is much higher and more variable than our typical single plume discharge. For the typical single plume case presented in figure 20, the density settles to about 10^{15} cm^{-3} with density fluctuations of about $\delta n/n \sim 0.1$. The low flux case exhibits density fluctuations of order unity.

In panel (e), we report the Mach flow ($M = v/c_s$) from the Mach probe, located about 1 cm from the wall of the wind tunnel (i.e. near the edge). The Mach number is of order unity consistent with a sound speed of 50 km s^{-1} and a $T_e + T_i = 30$ eV proton plasma. Fluctuations about the mean are also large (of order unity). From panel (f), we see that the ion temperature exhibits burstiness but has a mean value of about $T_i = 20$ eV. The SXR signal in panel (g) reflects the population of energetic electrons. Mach flow, ion temperature, and SXR are all measured at the midplane.

Figure 22 shows averaged time traces of the three main plasma parameters, B-field, edge Mach flow, and density presented in log-linear format in order to highlight exponential decay of the signal (which appears linear in this scaling). The magnetic data and the density data average 80 shots combining the 1.0 and 0.75 mWb runs. The Mach probe data has only 22 shots.

The blue lines indicate a best-fit exponential function for a region toward the end and beyond the typical analysis region. This shows that all three quantities exhibit exponential decay after plasma injection ceases. The density has the longest decay time so the plasma remains confined for longer than it has appreciable flows or magnetic fields. The flow fluctuations and the magnetic fields have essentially equal decay times. Since magnetic fields decay resistively and velocities decay viscously, the fact that magnetic fields and velocity fields decay at the same rate means that resistive and viscous diffusivities are similar in the SSX plasma wind tunnel, i.e. the magnetic Prandtl number $Pr = 1$. In practice, we have found that Prandtl numbers range from about Pr = 1–4.

We noted above that recording raw $\dot{B}$ data with a magnetic probe affords a higher bandwidth than using, for example, an active integrator circuit. Our analysis technique is to construct the spectrum for $\dot{B}$ (either FFT or wavelet), then divide the spectrum by f^2. Figure 23 shows a comparison of wavelet spectra constructed using raw $\dot{B}$ data that has been scaled by the square of the frequency in order to convert to B fluctuation spectra to time series data that is converted directly to B by performing numerical integration first. The numerical integration method might be expected to introduce some noise to the signal and potentially reduce the frequency resolution. Figure 23(a) shows that globally, the difference between the two forms of spectrum are very small. Figure 23(b) shows how the ratio of the two methods compare (with integrated spectrum over $\dot{B}$ spectrum). If the computed spectra were exactly alike, the ratio would be flat at 1.0. However, there is clearly some variation. The lines tend to drift upward at higher frequencies which is an indication of the noise introduced by integration method. However, the spectra do not deviate from one another by much more than 15–20%. While most of the analyzes are conducted using the $\dot{B}$ data, use of the integrated B data is nevertheless useful.

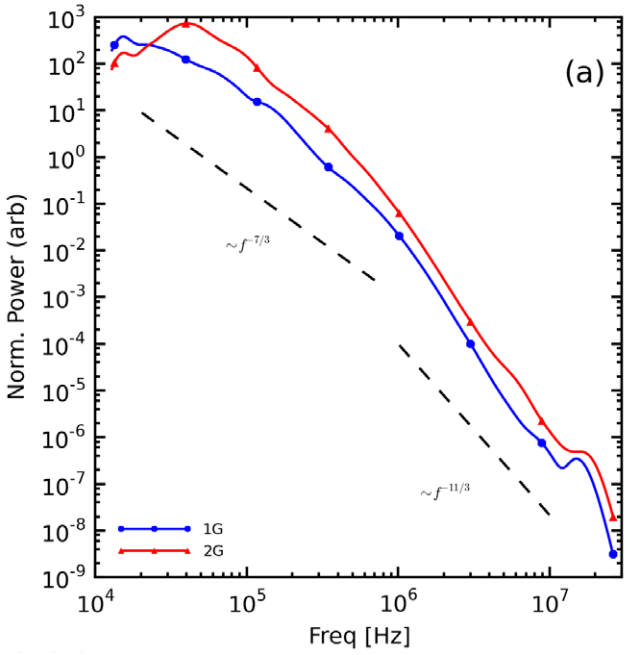

Figure 24. Comparison of spectra for merging versus single plume.

Virtually all of our initial analysis for the SSX MHD plasma wind tunnel has been for a single plume launched down the length of a cylindrical flux conserver. Relaxation of the unraveling flux rope drives MHD turbulence to small scales. High velocity merging of plasma plumes is more complicated. First, there is more total energy available for turbulence (a factor of two). Second, the flow is stagnated near the midplane driving reconnection and interpenetrating flows. Finally, the injection scale or the reservoir of energy to drive turbulence is modified. Figure 24 shows a plot of 1.0 mWb stuffing flux total magnetic fluctuation data for merging (red) and single plume (blue) datasets. Note that the two-gun power is overall larger and has a clear peak at 40 kHz. This could be reflective of a smaller injection size caused by the collision process, since the single plume data peaks at a lower frequency (larger scale).

While we have shown that varying the magnetic helicity of the MHD turbulent flow has a dramatic effect on intermittency [64], the time series and spectra are less sensitive to variations in other experimental quantities. Figure 25 shows total magnetic spectrum for changes in three different variables. In the first, single plume datasets are compared for discharge voltages of 4.0 and 3.5 kV. The shapes of the spectra are comparable, but the 3.5 kV discharge fluctuations actually have slightly more magnetic fluctuation energy than the 4.0 kV dataset. The second panel shows a scan of stuffing flux, 0, 0.5, 1.0 and 1.5 mWb, but for merging plumes rather than single plumes. As was the case for single plumes, the stuffing flux does not appear to modify the spectral shape, in the 100 kHz to 10 MHz range, but the 1.0 and 0.5 mWb datasets show slightly more spectral energy than the 0.0 and 1.5 mWb sets in that bandwidth. Since these are two gun runs, the peak in energy occurs at a higher frequency than the single gun. The third panel shows a comparison of gas delay timings which are a proxy for varying the amount of initial hydrogen gas present

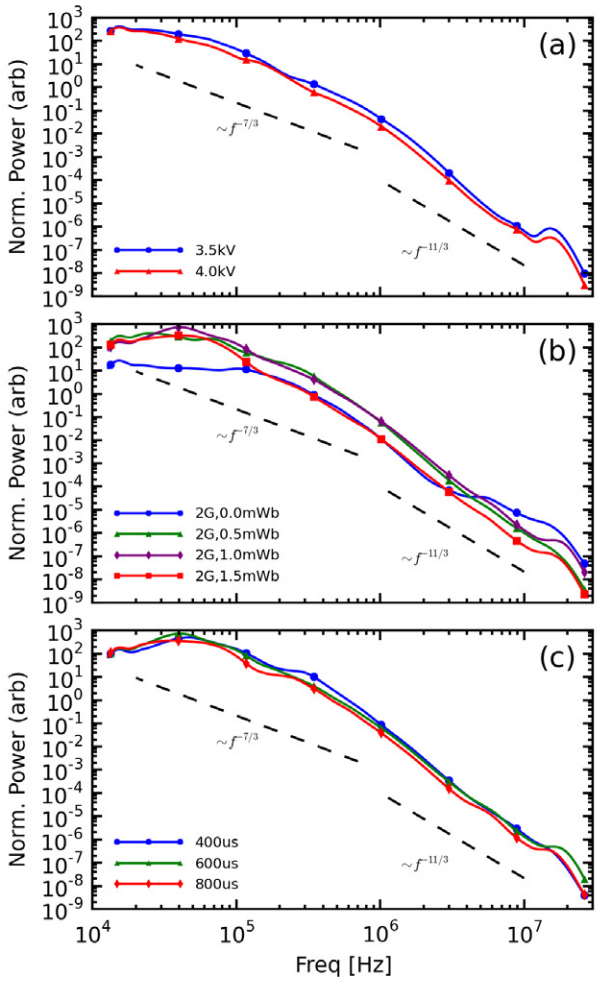

Figure 25. Comparison of spectra for three variables: (*a*) gun voltage; (*b*) gun flux; (*c*) gas load.

for the discharge, again for merging plume data. The spectra show very little variation, even less than the other scans. There does appear to be a slight inverse trend in overall fluctuation energy from long gas delay (red) to short gas delay (blue).

5. Conclusions

We have presented a review of laboratory sources of turbulent plasma, with a particular emphasis on MHD turbulence and on a new source called the SSX MHD plasma wind tunnel. Turbulence in devices designed for magnetic confinement fusion applications is strongly influenced by the strong applied toroidal (or axial) magnetic field. Natural plasmas often exhibit turbulence in which fluctuation energy in all dynamic quantities is comparable (magnetic, kinetic, thermal). The MHD plasma wind tunnel is an experimental approach to studying plasma turbulence more similar to that found in natural plasmas.

Acknowledgments

This work was supported by grants from the Department of Energy (OFES), and the National Science Foundation (Physics

Frontier Center for Magnetic Self Organization, CMSO). The authors gratefully acknowledge the assistance of technicians S Palmer and P Jacobs, and experimentalist students Adrian Wan '15, Peter Weck '15, Emily Hudson '17, Jeffrey Owusu-Boateng '16, Alexandra Werth '14, Darren Wienhold '12, Xingyu Zhang '12, Ken Flanagan '12, Bevan Gerber-Siff '10, Anna Phillips '10, Vernon Chaplin '07, and postdocs Tim Gray '01, Chris Cothran who all contributed to the SSX MHD wind tunnel.

References

[1] Batchelor G K 1970 *Theory of Homogeneous Turbulence* (Cambridge: Cambridge University Press)
[2] Frisch U 1995 *Turbulence: The Legacy of A N Kolmogorov* (Cambridge: Cambridge University Press)
[3] Kolmogorov A N 1941 *Dokl. Acad. Nauk. SSSR* **30** 301
[4] Bruno R and Carbone V 2013 *Living Rev. Solar Phys.* **10** 2
[5] Goldstein M, Roberts D and Matthaeus W 1995 *Annu. Rev. Astron. Astrophys.* **33** 283
[6] Tu C Y and Marsch E 1995 *Space Sci. Rev.* **73** 1
[7] Matthaeus W H *et al* 1995 *Rev. Geophys. Suppl.* **33** 609
[8] Liewer P C 1985 *Nucl. Fusion* **25** 543
[9] Zweben S J and Gould R W 1985 *Nucl. Fusion* **25** 171
[10] Bickerton R J 1997 *Plasma Phys. Control. Fusion* **39** 339
[11] Zweben S J *et al* 2007 *Plasma Phys. Control. Fusion* **49** S1
[12] Connor J W 1993 *Plasma Phys. Control. Fusion* **35** B293
[13] Rechester A B and Rosenbluth M N 1978 *Phys. Rev. Lett.* **40** 38
[14] Conway G D 2008 *Plasma Phys. Control. Fusion* **50** 124026
[15] Fonck R J *et al* 1993 *Phys. Rev. Lett.* **70** 3736
[16] Burrell K H 1997 *Phys. Plasmas* **4** 1499
[17] Burrell K H 1999 *Phys. Plasmas* **6** 4418
[18] Robinson D C and Rusbridge M G 1971 *Phys. Fluids* **14** 2499
[19] Terry P W *et al* 2012 *Phys. Plasmas* **19** 055906
[20] Ren Y, Almagri A F, Fiksel G, Prager S C, Sarff J S and Terry P W 2011 *Phys. Rev. Lett.* **107** 195002
[21] Grant H L, Stewart R W and Moilliet A 1962 *J. Fluid Mech.* **12** 241
[22] Matthaeus W H and Goldstein M L 1982 *J. Geophys. Res.: Space Phys.* **87** 10347
[23] Taylor G I 1938 *Proc. R. Soc. Lond.* A **164** 476
[24] Sahraoui F, Goldstein M, Robert P and Khotyaintsev Y 2009 *Phys. Rev. Lett.* **102** 231102
[25] Torrence C and Compo G P 1998 *Bull. Am. Meteorol. Soc.* **79** 6178
[26] Tsurutani B T and Smith E J 1979 *J. Geophys. Res.* **84** 2773
[27] Sorriso-Valvo L, Carbone V, Consolini G, Bruno R and Veltri P 1999 *Geophys. Res. Lett.* **26** 1801
[28] Greco A, Chuychai P, Matthaeus W H, Servidio S and Dmitruk P 2008 *Geophys. Res. Lett.* **35** L19111
[29] Greco A, Matthaeus W H, Servidio S, Chuychai P and Dmitruk P 2009 *Astrophys. J.* **691** L111
[30] Servidio S, Matthaeus W H and Dmitruk P 2008 *Phys. Rev. Lett.* **100** 095005
[31] Osman K T, Matthaeus W H, Greco A and Servidio S 2011 *Astrophys. J.* **727** L11
[32] Marsch E and Tu C Y 1997 *Nonlinear Process. Geophys.* **4** 101
[33] Kiyani K H *et al* 2009 *Phys. Rev. Lett.* **103** 075006
[34] Dyrud L *et al* 2008 *Nonlinear Process. Geophys.* **15** 847–62
[35] Belmabrouk H and Michard M 1998 *Exp. Fluids* **25** 69–76
[36] Matthaeus W H, Dasso S, Weygand J M, Milano L J, Smith C W and Kivelson M G 2005 *Phys. Rev. Lett.* **95** 231101
[37] Sahraoui F *et al* 2010 *Phys. Rev. Lett.* **105** 131101
[38] Servidio S *et al* 2011 *J. Geophys. Res.* **116** A09102
[39] Osman K T, Matthaeus W H, Hnat B and Chapman S C 2012 *Phys. Rev. Lett.* **108** 261103
[40] Osman K T, Matthaeus W H, Wan M and Rappazzo A F 2012 *Phys. Rev. Lett.* **108** 261102
[41] Bale S D, Kasper J C, Howes G G, Quataert E, Salem C and Sundkvist D 2009 *Phys. Rev. Lett.* **103** 211101
[42] Dudok de Wit T 2004 *Phys. Rev.* E **70** 055302
[43] Iroshnikov P S 1963 *Sov. Astron.* **7** 566
[44] Kraichnan R H 1865 *Phys. Fluids* **8** 1385
[45] Mininni P D and Pouquet A 2007 *Phys. Rev. Lett.* **99** 254502
[46] Mininni P D and Pouquet A 2009 *Phys. Rev.* E **80** 025401
[47] Podesta J J, Roberts D A and Goldstein M L 2007 *Astrophys. J.* **664** 543
[48] Schaffner D A *et al* 2012 *Phys. Rev. Lett.* **109** 135002
[49] Beall J M *et al* 1982 *J. Appl. Phys.* **53** 3933
[50] Holland C *et al* 2006 *Phys. Rev. Lett.* **96** 195002
[51] Toufen D L *et al* 2012 *Phys. Plasmas* **19** 012307
[52] Moser A L and Bellan P M 2012 *Nature* **482** 379
[53] Drummond W E and Rosenbluth M N 1962 *Phys. Fluids* **5** 1507
[54] Dorland W *et al* 2000 *Phys. Rev. Lett.* **85** 5579
[55] Zweben S J 1985 *Phys. Fluids* **28** 974
[56] White A E *et al* 2006 *Phys. Plasmas* **13** 072301
[57] Butt E P *et al* 1958 *Proc. 2nd Int. Conf. on Peaceful Uses of Atomic Energy (United Nations, Geneva)* vol 32, p 42
[58] Howes G G *et al* 2012 *Phys. Rev. Lett.* **109** 255001
[59] Brown M R 1999 *Phys. Plasmas* **6** 1717
[60] Gray T, Lukin V S, Brown M R and Cothran C D 2010 *Phys. Plasmas* **17** 102106
[61] Gray T, Brown M R and Dandurand D 2013 *Phys. Rev. Lett.* **110** 085002
[62] Bellan P M 2000 *Spheromaks* (London: Imperial College Press)
[63] Geddes C G R, Kornack T W and Brown M R 1998 *Phys. Plasmas* **5** 1027
[64] Schaffner D A, Wan A and Brown M R 2014 *Phys. Rev. Lett.* submitted
[65] Hutchinson I H 2002 *Principles of Plasma Diagnostics* 2nd edn (Cambridge: Cambridge University Press)
[66] Landreman M, Cothran C D, Brown M R, Kostora M and Slough J T 2003 *Rev. Sci. Instrum.* **74** 2361
[67] Cothran C D, Landreman M, Matthaeus W H and Brown M R 2003 *Geophys. Res. Lett.* **30** 1213
[68] Zhang X, Dandurand D, Gray T, Brown M R and Lukin V S 2011 *Rev. Sci. Instrum.* **82** 033510
[69] Johnson E O and Malter L 1950 *Phys. Rev.* **80** 58
[70] Buchenauer C J and Jacobson A R 1977 *Rev. Sci. Instrum.* **48** 769–74
[71] Chaplin V H, Brown M R, Cohen D H, Gray T and Cothran C D 2009 *Phys. Plasmas* **16** 042505
[72] Cothran C D, Fung J, Brown M R and Schaffer M J 2006 *Rev. Sci. Instrum.* **77** 063504
[73] Brown M R, Cothran C D, Gray T, Myers C E and Belova E V 2012 *Phys. Plasmas* **19** 080704
[74] Schaffner D A, Lukin V S, Wan A and Brown M R 2014 *Plasma Phys. Control. Fusion* **56** 064003